Received: 14 December 2020 | Revised: 1 July 2021 | Accepted: 7 July 2021

DOI: 10.1111/bre.12593

Basin Research IAS EAGE WILEY

RESEARCH ARTICLE

Detrital apatite geochemistry and thermochronology from the Oligocene/Miocene Alpine foreland record the early exhumation of the Tauern Window

Julian Hülscher[1] | **Edward R. Sobel**[2] | **Vincent Verwater**[1] | **Philip Groß**[3] | **David Chew**[4] | **Anne Bernhardt**[1]

[1]Institute of Geological Sciences, Freie Universität Berlin, Berlin, Germany

[2]Institut für Geowissenschaften, Universität Potsdam, Potsdam-Golm, Germany

[3]Institut für Geowissenschaften, Universität Heidelberg, Heidelberg, Germany

[4]Department of Geology, School of Natural Sciences, Trinity College Dublin, Dublin, Ireland

Correspondence
Julian Hülscher, Institute of Geological Sciences, Tectonics and Sedimentary Systems, Freie Universität Berlin, Malteserstr. 74-100, 12249 Berlin, Germany.
Email: julian.huelscher@fu-berlin.de

Funding information
Science Foundation Ireland; Deutsche Forschungsgemeinschaft

Abstract

The early exhumation history of the Tauern Window in the European Eastern Alps and its surface expression is poorly dated and quantified, partly because thermochronological and provenance information are sparse from the Upper Austrian Northern Alpine Foreland Basin. For the first time, we combine a single-grain double-dating approach (Apatite Fission Track and U-Pb dating) with trace-element geochemistry analysis on the same apatites to reconstruct the provenance and exhumation history of the late Oligocene/early Miocene Eastern Alps. The results from 22 samples from the Chattian to Burdigalian sedimentary infill of the Upper Austrian Northern Alpine Foreland Basin were integrated with a 3D seismic-reflection data set and published stratigraphic reports. Our highly discriminative data set indicates an increasing proportion of apatites (from 6% to 23%) with Sr/Y values <0.1 up-section and an increasing amount of apatites (from 24% to 38%) containing >1,000 ppm light rare-earth elements from Chattian to Burdigalian time. The number of U-Pb ages with acceptable uncertainties increases from 40% to 59% up-section, with mostly late Variscan/Permian ages, while an increasing number of grains (10%–27%) have Eocene or younger apatite fission track cooling ages. The changes in the apatite trace-element geochemistry and U-Pb data mirror increased sediment input from an ≥upper amphibolite-facies metamorphic source of late Variscan/Permian age – probably the Ötztal-Bundschuh nappe system – accompanied by increasing exhumation rates indicated by decreasing apatite fission track lag times. We attribute these changes to the surface response to upright folding and doming in the Penninic units of the future Tauern Window starting at 29–27 Ma. This early period of exhumation (0.3–0.6 mm/a) is triggered by early Adriatic indentation along the Giudicarie Fault System.

KEYWORDS

detrital apatite fission track analysis, detrital apatite trace-element geochemistry, Molasse Basin, Northern Alpine Foreland Basin, Tauern Window

1 | INTRODUCTION

The exhumation of the Tauern Window in the European Eastern Alps has long been interpreted to have started in late Oligocene/early Miocene times (Blanckenburg et al., 1989; Frisch et al., 1998; Ratschbacher et al., 1991). However, other studies postulate Oligocene exhumation from ca. 28 Ma onwards based on bedrock cooling ages from the exposed Tauern Window (Favaro et al., 2015; Reddy et al., 1993; Schneider et al., 2015). The erosional products of this early exhumation period have not yet been recognized, particularly because thermochronological and provenance constraints from the most proximal sedimentary records in the eastern Northern Alpine Foreland Basin (NAFB) in Upper Austria (Figures 1 and 2) are sparse (Brügel et al., 2003; Kuhlemann et al., 2006; Sharman et al., 2018). In this study, we examine provenance and erosional history information from apatites by combining a single-grain double-dating approach (fission track [AFT] and U-Pb dating) with analysis of the apatite trace-element geochemistry (ATE) on the same grain. This multi-proxy dataset on the same mineral phase allows us to constrain the evolution of individual grains from the protolith conditions under which the apatite grew (ATE; O'Sullivan et al., 2020), to the timing of the last medium-temperature event (U-Pb dating; closure temperature: 375–550°C; Chamberlain and Bowring, 2001) and the exhumation of the grain into shallow (ca. 3–4 km) crustal levels (AFT; closure temperature: 120 ± 20°C; Reiners & Brandon, 2006).

The Upper Austrian NAFB (Figure 1) offers an excellent opportunity to constrain the Eastern Alpine evolution because extensive complementary datasets are available, including a large scale (>6,400 km^2, >5 km depth) 3D seismic-reflection dataset and comprehensive stratigraphic reports (Grunert et al., 2013, 2015; Hülscher et al., 2019) (Figure 2). We focus on the Chattian to Burdigalian infill of the basin (Figure 2; 27.5–18.3 Ma; Hülscher et al., 2019) and have sampled drill cores provided by RAG Austria AG (Vienna) who also provided the 3D seismic dataset. The linkage of apatite geochemistry and thermochronology, seismic interpretation and bio- and chemostratigraphic information in the sedimentary sink enables us to constrain the provenance of the sediments in the Upper Austrian NAFB (Figures 1 and 2). Furthermore, we date and quantify the early exhumation of the Tauern Window from 29 to 27 Ma onwards, which has caused exhumation (0.3–0.6 mm/a) and denudation of the overlying Upper Austroalpine units, triggered by Adriatic indentation along the Giudicarie Fault System (Cliff et al., 1985; Favaro et al., 2015; Reddy et al., 1993).

Highlights

- Provenance and low-T thermochronology approach applied together on detrital apatites.
- Apatites analyzed for U-Pb ages, AFT ages, and trace-element geochemistry.
- Oligocene Tauern Window exhumation for the first time dated and quantified from the detrital record.
- Slow (0.3–0.6 mm/a), early (29–27 Ma) Tauern exhumation accelerates after 21 Ma.

2 | APATITE AS A PROVENANCE AND THERMOCHRONOLOGY TOOL

Apatite ($Ca_5(PO_4)_3(OH, F, Cl)$) is a common mineral in igneous, metamorphic and sedimentary rocks. Based on the highly diverse apatite-trace element abundances (REE, Sr, Mn, Y, Th, U) that is controlled by the protolith geochemistry and the metamorphic/magmatic conditions the mineral grew in (Belousova et al., 2001, 2002; Henrichs et al., 2018), O'Sullivan et al. (2020) built the first widely applicable source-rock discrimination diagram. Discrimination is based on three trends identified from a compiled literature data set. (1) The light rare-earth elements (LREE [La to Nd]) content is low in low-grade metamorphic rocks, increases with the metamorphic grade and is accompanied by a corresponding decrease in the Sr/Y ratio. (2) The Sr and Y contents of magmatic apatite negatively correlate and positively correlate with the SiO_2 content of the source melt, respectively; the exception is apatite from alkali-rich melts, which is instead recognized by its extremely high LREE-contents. (3) Dissolution and reprecipitation of apatite under low-grade metamorphic conditions will result in a LREE-depleted apatite with a high Sr/Y ratio. O'Sullivan et al. (2020) separated the

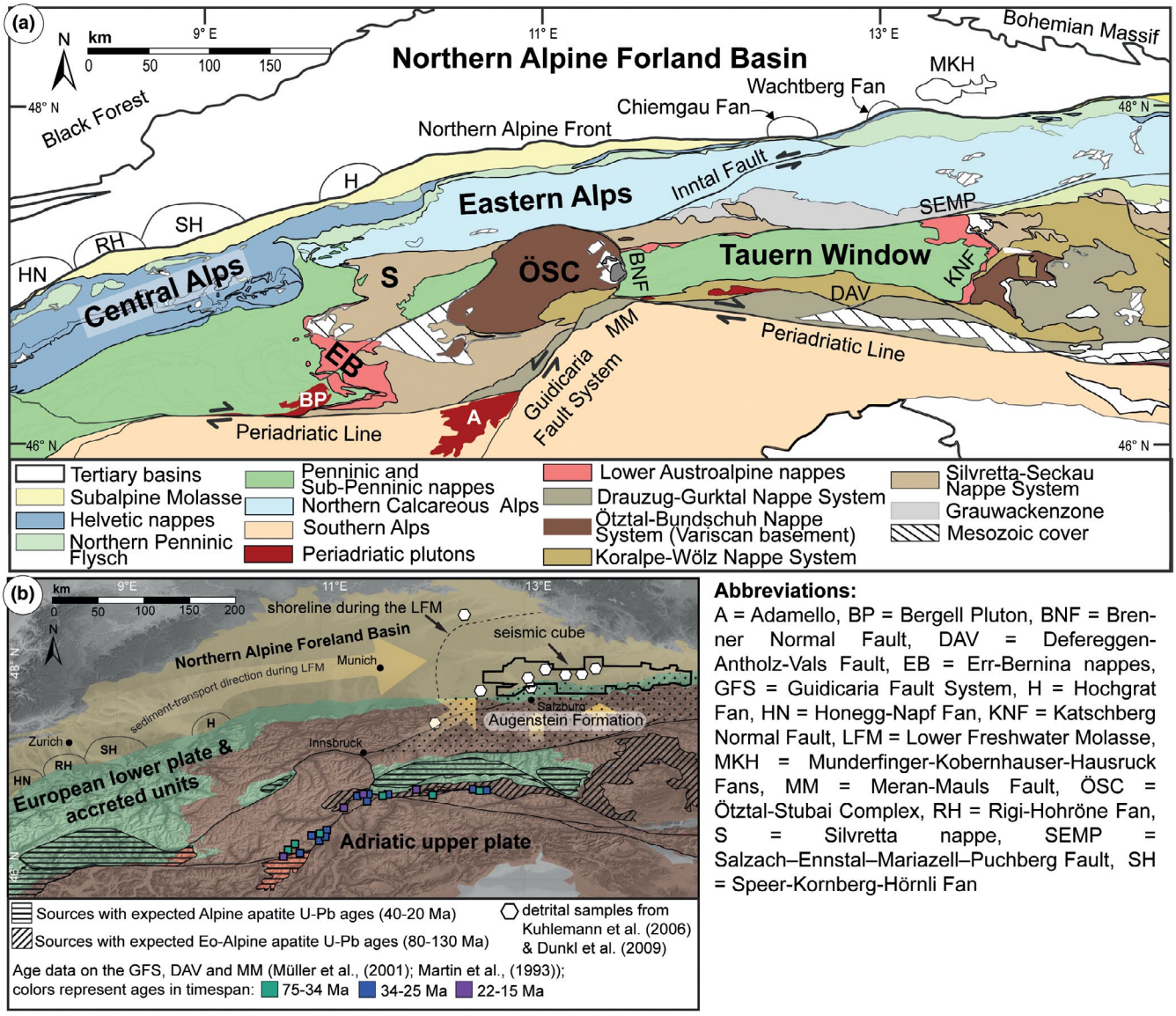

FIGURE 1 Simplified geological (a) after Schmid et al. (2004) and geographical (b) maps of the Central and Eastern European Alps. Note in (b) the sample locations of publications detailed in the text and the position of the 3D seismic cube. Symbols of the sample localities partly represent two samples that were taken very close to each other. Dashed areas in (b) are regions of upper greenschist-facies and higher grade metamorphism from Bousquet et al. (2012). Extent of the AFM in (b) after Frisch et al. (2001); sediment-transport direction in the NAFB after Füchtbauer (1964)

literature data set into six classes of source rocks (alkali-rich igneous rocks [ALK]; mafic I-type granitoids and mafic igneous rocks [IM]; low- and medium-grade metamorphic [<upper amphibolite-facies] and metasomatic [LM]; partial-melts/leucosomes/high-grade metamorphic [HM]; S-type granitoids and high aluminum saturation index [>1.1] 'felsic' I-types [S]; ultramafic rocks including carbonatites, lherzolites and pyroxenites [UM]) using Principle Component Analysis and applied a machine-learning classifier method to define decision-boundaries on a log(∑LREE ppm) versus log(Sr/Y) diagram. The correct classification of this separation based on the training dataset is on average ca. 85% per class (O'Sullivan et al., 2020).

Dating of detrital apatite via the U-Pb system has increased significantly in the last decade with the development of high throughput LA-Q-ICP-MS analyses and correction procedures for age reference materials with variable common Pb (Chew et al., 2014). The apatite U-Pb thermochronometer records medium-temperature metamorphic/magmatic events (375–550°C; Chamberlain & Bowring, 2001). However, apatites with low U concentrations («1 ppm) and/or high common Pb contents (Pb_c) are typically not datable (Henrichs et al., 2018; O'Sullivan et al., 2018).

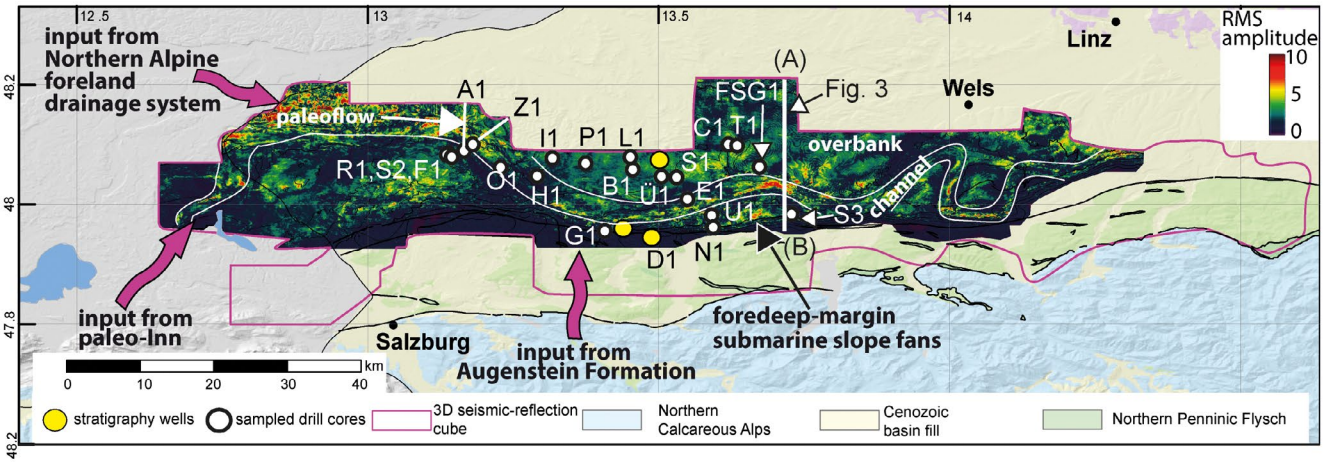

FIGURE 2 Simplified geological map of the Upper Austrian NAFB showing the locations of the sampled drill cores and of the three wells with published stratigraphic information (Hülscher et al., 2019). The pink outline shows the extent of the 3D-seismic cube provided by the RAG. The inset shows a root mean square amplitude map of the seismic-reflection surface of the Base Hall Unconformity outlining the axial channel, the extensive overbank deposits on the northern basin margin and the slope fans on the southern tectonically active margin. Note that the channel meanders migrated through the basin over time (Figure 3). See Table S2 for coordinates of the samples

In ancient sedimentary systems, the lag-time approach can be applied to reconstruct the exhumation of the orogenic hinterland. To calculate lag times, the absolute depositional age of the sample is subtracted from the AFT age (Garver et al., 1999). Lag times integrate the time over which the grain was exhumed from depth, eroded, transported and deposited into the sink. Changes in hinterland exhumation rates are recorded by decreasing (increasing exhumation rate), increasing (decreasing exhumation rate) or constant (constant exhumation rate) lag times, as long as post-depositional annealing in the sedimentary sink can be ruled out as a source of dispersion (Bernet, 2019). Syn-depositional volcanic activities can also complicate cooling age distributions as they deliver young, fast-cooled grains (Carter, 2019). Furthermore, interpreting detrital thermochronological datasets in terms of hinterland exhumation can be hampered by provenance changes (Malusà & Fitzgerald, 2019). By combining ATE and U-Pb analysis with AFT analysis, we avoid these potential biases as we can constrain the provenance and the exhumation history of the apatites independently and thus exclude syn-depositional volcanic apatite grains.

3 | GEOLOGICAL SETTING

3.1 | The Upper Austrian Northern Alpine Foreland Basin

The NAFB is the Cenozoic pro-wedge foreland basin of the central European Alpine orogen. It extends ca. 1,000 km from Switzerland to Austria (Figure 1) (west–east) and up to 120 km in a north–south direction (Kuhlemann & Kempf, 2002). In contrast with the fluvial conditions in the German and Swiss NAFB during the Lower Freshwater Molasse (28–20 Ma), the Austrian part of the basin (Figure 1) remained deep marine (water-depth >1,000 m; Rögl et al., 1979). During the deposition of the Zupfing Formation (29.6–26.9 Ma; Hülscher et al., 2019), a 3–6 km wide, gravity-flow dominated channel system developed flowing parallel to the Alpine front from west to east for >100 km (Figures 2 and 3; De Ruig & Hubbard, 2006). This channel controlled sedimentation in the basin during the deposition of the Puchkirchen Group (Lower [LPF] and Upper Puchkirchen Formation [UPF]; 26.9–19.6 Ma) and the basal Hall Formation (19.6–19.0 Ma; Hülscher et al., 2019). In the channel, sandstones, conglomerates and silty marls were deposited by turbidity currents, debris flows and hemipelagic suspension settling (Bernhardt et al., 2012; De Ruig & Hubbard, 2006; Hubbard et al., 2009). To the north, the channel is bounded by wide (≤15 km) overbanks (Figure 2) where dominantly silty-marls and fewer turbiditic sandstones occur (Hubbard et al., 2009; Masalimova et al., 2015). The southern basin margin was tectonically active and submarine fans prograded from the south northwards into the basin (Covault et al., 2009; Hinsch, 2008). The channel and the northern overbanks received sediment from the Central and Eastern Alps, whereas the southern slope was mainly built up by detritus sourced from the Eastern Alps (Sharman et al., 2018). Two basin-wide unconformities have been described in the Upper Austrian NAFB (Figure 3): the

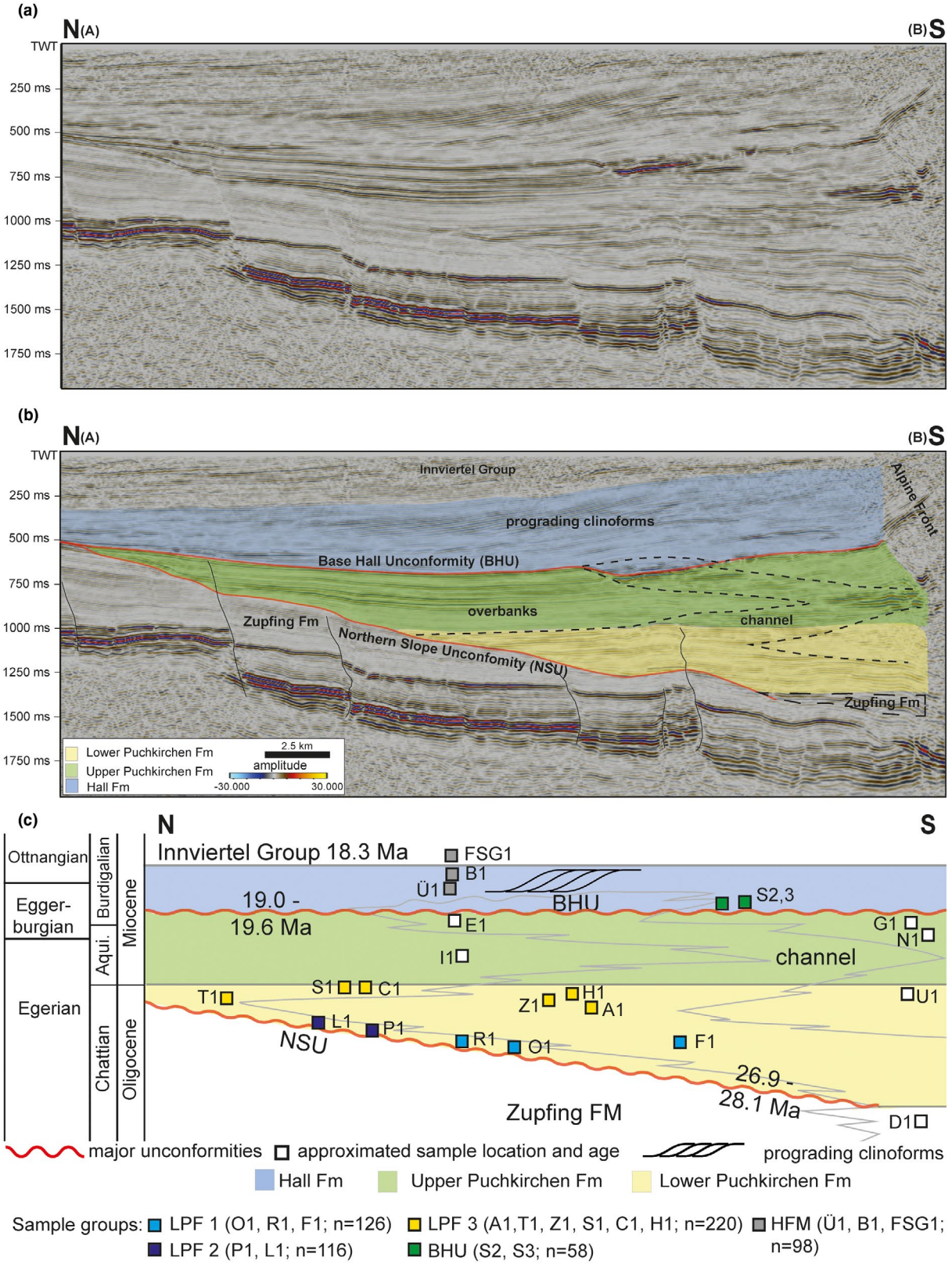

FIGURE 3 Seismic cross-section (N-S) through the Upper Austrian NAFB (see Figure 2 for position). Note the lateral mobility of the main channel belt and the wide northern overbanks. (a) Uninterpreted, (b) interpreted cross-section. (b) The main channel belt and both unconformities are highlighted; the stratigraphic framework is taken from Hülscher et al. (2019). (c) Schematic stratigraphy in the basin with the sampled drill cores projected onto the wells with bio- and chemostratigraphic information (Figure 2). Note the colour coding of the grouped samples; white samples do not belong to any sample group and are interpreted independently. Aqui. = Aquitanian; *n* = number of grains in the grouped samples

Northern Slope Unconformity (NSU, established between 28.1 and 26.9 Ma) and the Base Hall Unconformity (BHU, established ca. 19.6 Ma) which marks the beginning of the Upper Marine Molasse (De Ruig & Hubbard, 2006; Hülscher et al., 2019; Masalimova et al., 2015).

A sea-level highstand at ca. 19 Ma caused the termination of channel sedimentation in the Hall Formation (HFM; Grunert et al., 2013) and the sediment-routing system changed to northward sediment transport (Hülscher et al., 2019). This marine incursion in the NAFB (Upper Marine Molasse) resulted in a cut-off of the sediment supply from the Central Alps to the Upper Austrian NAFB (Kuhlemann & Kempf, 2002). Thereafter, clinoforms started to prograde from the south into the basin and filled it up to water depths of <200 m until 18.3 Ma (Figure 3; Grunert et al., 2013). The HFM is overlain by the Innviertel Group of Ottnangian age which represents the terminal stage of marine Molasse sedimentation (Grunert et al., 2012).

3.2 | The Alpine orogenic hinterland

The present-day Alps are the product of a continent-continent collision between the European plate in the north and the Adriatic microplate in the south. Southward subduction of the Penninic Ocean underneath the Adriatic upper plate initiated in the Late Cretaceous and led to the northward drift of Adria, ultimately resulting in collision around 35 Ma (Handy et al., 2010). This led to a widespread high-pressure metamorphic overprint in the subducted rocks of the lower plate in Paleogene times (Figure 1) and the nappe stacking of three mega-units (from bottom to top; Schmid et al., 2004):

1. The Helvetic nappes (crystalline basement of the European distal margin and its overlying sedimentary cover).
2. The Penninic nappes (magmatic and sedimentary rocks of the former Alpine Tethys ocean which experienced subsequent Alpine greenschist- to eclogite-facies metamorphism) and
3. The Austroalpine nappes (Variscan greenschist to eclogitic-facies metamorphic and magmatic basement rocks and their post-Variscan sedimentary cover) as part of the upper Adriatic plate (Schmid et al., 2004). The Austroalpine units can be further subdivided into Upper (Drauzug-Gurktal, Ötztal-Bundschuh, Koralpe-Wölz and Silvretta-Seckau Nappe Systems) and Lower Austroalpine nappes (e.g. Err-Bernina Nappe, Radstadt Tauern units). The Koralpe-Wölz Nappe System experienced an Eoalpine (120–60 Ma) amphibolite to eclogite-facies metamorphic overprint when it was subducted underneath the Drauzug-Gurktal and Ötztal-Bundschuh nappe systems (Schmid et al., 2004).

Sedimentary and metagranitic Lower Austroalpine nappes covered the Central Alps until the early Miocene (Spiegel et al., 2001). Only from ca. 21 Ma onwards, Penninic units were exposed and their material reached the alluvial fans in the Swiss NAFB (Spiegel et al., 2001). From there, sediments were transported by an east-directed river network (Füchtbauer, 1964) to a delta system east of Munich (Zweigel, 1998) which fed the Puchkirchen channel system (Sharman et al., 2018).

A large part of the Eastern Alps was drained in Oligocene and Miocene times via the paleo-Inn river system through the Inn valley (Figure 1) to the Chiemgau, Wachtberg and Munderfinger-Kobernhauser-Hausruck (MKH) fans (Brügel et al., 2003). The first Penninic pebbles from the then opened Tauern Window appear in these deposits at ca. 13 Ma (Brügel et al., 2003). AFT analysis of the paleo-Inn deposits revealed a shortening of lag times from Rupelian to early Aquitanian deposits and short lag times thereafter (Dunkl et al., 2009; Kuhlemann et al., 2006). The drainage network of the paleo-Inn system must have reached the magmatic sources along the Periadriatic Line, as evident by Eocene and Oligocene U-Pb zircon and K-Ar pebble ages in the Upper Austrian NAFB sediments (Brügel et al., 2000; Sharman et al., 2018). In Miocene times, the Err-Bernina nappes were probably drained by the paleo-Inn (Skeries & Troll, 1991).

From 35 to 30 Ma onwards, the ≤2 km thick Augenstein Formation (AFM) accumulated on top of today's Northern Calcareous Alps, east of the Inntal fault (Figure 1; Frisch et al., 2001). It was sourced from the Austroalpine basement (Figure 1) and its Mesozoic cover in the south (Frisch et al., 2001; Ortner & Stingl, 2001). Rivers that transported this material must have crossed the AFM from south to north, ultimately entering the Upper Austrian NAFB and depositing their material on the southern slope (Frisch et al., 1998; Sharman et al., 2018). At ca. 21 Ma, the initiation of uplift of the Northern Calcareous Alps resulted in the erosion and redeposition of the AFM into the Upper Austrian NAFB (Frisch et al., 2001).

4 | SAMPLES AND METHODS

Samples (0.7–2.2 kg) were taken from 17 drill cores and were augmented by one outcrop sample (Figure 2, Table 1). The depositional age of the samples ranges between 27.5 and 18.3 Ma (Figure 3, Table 1). We sampled turbiditic, fine-to-coarse sand overbank deposits on the northern and southern slopes of the Upper Austrian NAFB. Each drill core was correlated within the 3D seismic reflection

TABLE 1 Sampled drill cores and outcrop in the Upper Austrian NAFB and the results from the ATE, U-Pb and AFT analysis

Sample	Depositional age	Uncertainty	Depositional setting	Stratigraphic position	Samples sieved at	Apatites for trace element geochemistry	Accepted apatite U-Pb ages	Grains dated via AFT	Central age (Ma)	AFT analysis conducted at	Results χ^2-test	AFT ages of volcanic origin	Apatites classified as				
													LM	HM	IM	S	UM
D1	27.5	0.5	Main channel belt	ZFM	—	34	10	—	—	—	—	—	21	3	9	1	—
O1	24.5	0.1	Northern Overbanks	LPF	—	74	25	39	65.8 (±4.3)	UP	0	—	50	9	12	—	3
R1	24.3	0.1	Northern Overbanks	LPF	—	33	21	15	60.5 (±9.3)	FUB	0	2	13	10	10	—	—
F1	24.4	0.2	Main channel belt	LPF	—	19	6	9	71 (±15)	FUB	0	—	15	3	1	—	—
LPF1	**24.3**	**0.2**		**LPF**		**126**	**52**	**63**			**0**		**78**	**22**	**23**	**0**	**3**
P1	24.2	0.1	Northern Overbanks	LPF	—	40	12	22	64.9 (±9.3)	UP	0	1	27	6	5	1	1
L1	24.1	0.1	Northern Overbanks	LPF	>100 µm	76	27	42	53.8 (±4.3)	FUB	0	—	47	18	9	2	—
LPF2	**24.1**	**0.2**		**LPF**		**116**	**39**	**64**			**0**		**74**	**24**	**14**	**3**	**1**
A1	23.2	0.3	Main channel belt	LPF	—	29	15	10	70 (±12)	FUB	0	—	12	4	9	2	2
T1	23.5	0.2	Northern Overbanks	LPF	<100 µm	26	14	14	61.7 (±5.3)	FUB	0.57	—	13	6	7	—	—
Z1	23.1	0.2	Main channel belt	LPF	—	41	13	8	35.9 (±6.1)	FUB	0.01	—	15	8	14	4	—
S1	23.2	0.1	Northern Overbanks	LPF	<100 µm	72	51	40	50.9 (±4.7)	UP	0	—	25	23	12	11	1
C1	23.2	0.1	Northern Overbanks	LPF	<100 µm	27	18	16	58.5 (±5.3)	FUB	0.15	—	8	11	4	4	—
H1	23.2	0.3	Main channel belt	LPF	—	25	5	7	43.4 (±6.8)	FUB	0	—	13	3	8	1	—
LPF3	**23.3**	**0.3**		**LPF**		**220**	**116**	**95**			**0**		**86**	**55**	**54**	**22**	**3**
I1	**22.2**	**0.2**	**Northern Overbanks**	**UPF**	—	**77**	**39**	**55**	**52.2 (±5.1)**	**FUB**	**0**	—	**28**	**23**	**14**	**9**	**3**
E1	**20**	**0.4**	**Main channel belt**	**UPF**	>100 µm	**153**	**62**	**103**	**46.4 (±2.6)**	**FUB/UP**	**0**	—	**74**	**52**	**19**	**7**	**1**
S2	19.3	0.3	Southern Overbanks	Basel HFM	—	20	11	12	66 (±12)	FUB	0	—	5	11	3	1	—
S3	19.3	0.3	Southern Overbanks	Basel HFM	—	38	29	30	55.5 (±6.3)	FUB	0	—	2	20	11	5	—
BHU	**19.3**	**0.3**				**58**	**40**	**42**			**0**		**7**	**31**	**14**	**6**	**0**
Ü1	18.8	0.2	Prograding Clinoform	HFM	—	27	16	23	59.2 (±7.4)	FUB	0.02	—	12	10	3	2	—
B1	18.6	0.2	Prograding Clinoform	HFM	—	41	23	29	55.1 (±7.5)	UP	0	—	17	14	3	5	2
FSG1	18.3	0.1	Tidal influenced, nearshore	Atzbach Formation (Innviertel Group)	—	30	18	16	51.8 (±6.6)	FUB	0	—	7	14	6	2	1
HFM	**18.6**	**0.3**	**HFM**			**98**	**57**	**68**			**0**		**36**	**38**	**12**	**9**	**3**
U2	23.1	1	Southern Overbanks	LPF	<100 µm	19	9	10	51.5 (±7.8)	FUB	0.03	1	9	5	5	—	—
N1	21.5	0.5	Southern slope fan	UPF	—	44	24	26	56.3 (±6.3)	FUB	0	—	15	15	10	2	2
G1	20.8	0.2	Southern slope fan	UPF	—	77	18	45	63 (±4)	FUB	0	1	47	9	20	—	1

Note: Six samples were sieved before mounting; the mounted grain-size fraction is indicated. Note that no trend towards younger AFT central ages is visible down-section (Figure S5). This indicates that post-depositional annealing in the basin by burial of the material does not represent a significant source of dispersion in the results. For coordinates of the individual samples see Table S2. Bold lines represent grouped samples from the northern slope.

Abbreviations: FUB, FU Berlin; UP, University of Potsdam.

cube (seismic reflectors were mapped as timelines; vertical resolution of each reflector is ca. 33 m; Figure S1) onto at least one of the three wells with bio- and chemostratigraphic information in the area to constrain the depositional ages (Figure 2, Table 1; Hülscher et al., 2019). In general, we excluded intra-channel deposits because the erosional channel prevents stratigraphic correlation (Hubbard et al., 2009). However, to fill the temporal gap between samples I1 and S2,3 (ca. 3 Myr, Figure 3) we collected one channel-fill sample (E1), due to the lack of contemporaneous overbank samples. Four samples (H1, Z1, A1, F1) from channel deposits were included which previously were analysed by Hejl and Grundmann (1989). For these five channel samples, we chose a seismic reflector of similar depth on the overbank side at the channel-overbank boundary. This results in larger uncertainties on the depositional ages of these samples (Table 1). To increase the statistical significance, stratigraphically close samples were grouped together (Table 1, Figure 3).

4.1 | Sample preparation and fission track methodology

Samples were crushed and the apatites were separated following the protocol of Kohn et al. (2019). Six samples were then sieved to further increase the proportion of apatite (Table 1). Apatite concentrates were prepared for irradiation by mounting the samples with epoxy resin on a glass plate, which was followed by grinding, polishing and etching of the mounts (following Carlson et al., 1999; 5.5 M HNO_3 for 20 s at 21°C). We used the external detector method following Gleadow (1981) for AFT dating with the zeta-calibration method (Hurford & Green, 1983) and CN5 as dosimeter glass for neutron flux monitoring during sample irradiation. The samples from Hejl and Grundmann (1989) were originally dated with the population method (Naeser, 1979) and etched with 5% HNO_3 for 45 s at 21°C. To date the individual grains, the grain mounts were covered with the dosimeter glass and reirradiated. After irradiation, the mica external detectors were etched with 40% HF for 45 min at 21°C. The density of spontaneous and induced tracks of the individual grains was measured at the University of Potsdam with a Leica DMR microscope and at the Freie Universität Berlin with a Zeiss Axioplan 2 microscope (Table 1).

Single-grain AFT ages were calculated with MacTrackX. After evaluating the results from the ATE and U-Pb analysis (see below), all grains with an Alpine magmatic origin (plot in the IM-field; U-Pb ages between 21 and 60 Ma) were excluded from the fission track population to avoid obscuring the orogenic cooling history by magmatic detritus with cooling ages close to the depositional ages (Bernet, 2019). Grain-age populations were calculated using the automatic mixture modelling software RadialPlotter (Vermeesch, 2009) but only for the northern slope samples due to the small number of AFT-dated grains from the southern slope samples. In a second step, grains were grouped by their U-Pb ages into two subgroups: one subgroup with Variscan and Permian U-Pb ages (400–250 Ma, hereafter termed the Variscan subgroup) and a second subgroup with U-Pb ages <250 and >400 Ma and all grains where U-Pb dating failed (hereafter termed the non-Variscan subgroup). For both subgroups, individual grain-age populations were calculated. Lag times (Garver et al., 1999) were calculated by subtracting the depositional ages of the grouped samples from the AFT ages (Tables 1 and 2). Based on the calculated lag times, exhumation rates were calculated. We assumed 120 ± 20°C as the AFT closure temperature (Reiners & Brandon, 2006) based on the measured Dpar values (Figure S2) and an assumed geothermal gradient of 30°C/km (Fügenschuh et al., 2000) for the Upper Austroalpine nappes. All uncertainties associated with the AFT data are at the 1σ level.

4.2 | Single grain LA-ICP-MS analyses

Analysis of the ATE and U-Pb isotopic compositions were carried out during the same analytical session at Trinity College Dublin, Ireland, using a Teledyne Photon Machines Analyte Excite 193 nm ArF Excimer laser-ablation system coupled to a Thermo Scientific iCAP-Q ICP-MS. The individual apatite grains were ablated with the laser using a 30 μm spot size, a 13 Hz repetition rate and a fluence of ca. 3.5 J/cm^2. He carrier gas flow (650 ml/min) was split evenly between the larger outer and smaller inner sample chamber where grains were ablated. N_2 (ca. 6 ml/min) and Ar nebulizer gas (700 ml/min) were introduced to the sample gas via an in-house smoothing device to enhance signal sensitivity and reduce oxide formation. We used the ca. 473 Ma Madagascar apatite standard (Thomson et al., 2012) as the primary reference material for the U-Pb geochronology. The U-Pb standards Durango apatite (31.44 ± 0.18 Ma; McDowell et al., 2005); this study Tera-Wasserburg (TW) lower-intercept age of 31.2 ± 1.2 Ma, $n = 69$, MSWD = 1.8) and McClure Mountain apatite ($^{207}Pb/^{235}U$ TIMS age of 523.51 ± 1.47 Ma; Schoene and Bowring (2006); this study TW lower-intercept age of 527.0 ± 4.0 Ma, $n = 139$, MSWD = 3.9) were employed as secondary age standards. NIST612 was used as the primary reference material for the trace element analysis.

Raw data reduction was performed with VisualAge_UcomPbine (Chew et al., 2014) within the freeware IOLITE package (Paton et al., 2011). To correct for Pb_c

in the apatite primary standard, a ^{207}Pb-based correction method was applied that used an initial ^{207}Pb/^{206}Pb ratio from the Stacey and Kramers (1975) terrestrial Pb isotope evolution model. For the unknowns, the iterative ^{207}Pb-based correction introduced by Chew et al. (2011) was used. Due to the ^{207}Pb-correction, a discordance-based exclusion of U-Pb ages is not applicable. Therefore, we set an arbitrarily chosen limit of acceptance for uncertainties on U-Pb ages with 2σ uncertainties <25% for ages >100 Ma and <50% for ages <100 Ma. All uncertainties associated with the U-Pb data are quoted at the 2σ level. The results of the ATE were plotted and characterized with the discrimination diagram introduced by O'Sullivan et al. (2020) in the 'R' environment.

To test whether the LREE and Sr/Y single-grain distributions of different samples result from random sampling of the same parent population or are significantly different, we performed a Kolmogorov–Smirnov (K–S) test (Hodges, 1958). This non-parametric test is based on the maximum difference (D) of the cumulative distribution function of the two samples. Based on D, it computes a likelihood (p) whether the compared samples are taken from the same population (H0-hyphothesis) or not. We reject the H0-hyphothesis in cases where p is <5%.

5 | RESULTS

5.1 | Apatite trace element geochemistry and U-Pb analysis

Thousand and twenty-two apatite grains were analysed for their trace-element geochemistry and U-Pb ages (Table 1, Figures 4–6). In the oldest sample D1 (depositional age: 27.5 ± 0.5 Ma), 34 apatites were analysed (Figure S3). The LREE content in these grains ranges between 100 and 10,000 ppm and the Sr/Y values vary between 0.1 and 10. Plotted on the discrimination diagram of O'Sullivan et al. (2020), the apatites indicate both IM and LM sources.

The northern slope sample groups LPF1 and LPF2 (Figures 3 and 4a,b, Table 1) are statistically indistinguishable (Table S1). Both contains apatites with LREE values mostly below 1,000 ppm (76% LPF1, 80% LPF2) and Sr/Y ratios above 0.1 (94% LPF 1, 89% LPF2). Within the biplot classification of O'Sullivan et al. (2020), grains plot in the LM-field (60%–64%), IM-field (18%–12%) and in the HM-field (17%–21%). Uncertainties related to misclassified apatites based on the success rate of the discrimination (O'Sullivan et al., 2020) are shown in Figure 6.

The sample groups LPF3 I1, E1 and HFM (Figures 3 and 4, Table 1) show an increase in the absolute number of apatites with a LREE content >1,000 ppm (39% LPF3, 47% I1, 35% E1, 38% HFM) and Sr/Y values below 0.1 (20% LPF3, 24% I1, 21% E1, 23% HFM). The samples differ significantly from the samples LPF1 and LPF2 (p < 5% for Sr/Y of all samples and p < 5% for LREE content of all samples except for E1 and LPF2 where p = 9%, Table S1). Most apatites are still characterized as LM apatites (36%–49%) but the abundance of HM apatites increases (25%–38%, Figure 6). IM-type (12%–25%) and S-type grains are a minority in the samples (5%–12%, Figure 4).

The sample group BHU (S2, S3, Figures 3 and 4f, Table 1) contains 58 apatites. Twenty-one grains have LREE values below 1,000 ppm (36%) and 20 grains (34%) show Sr/Y values below 0.1. The K–S test results suggest that this sample group is unlikely to be drawn out of the same distribution as the remaining samples (p < 5%, Table S1). Most grains plot in the discrimination diagram in the HM- (53%) and IM-field (24%). Twelve per cent of the apatites have an LM affinity and 10% have S-type characteristics (Figure 6).

The oldest sample on the southern slope U1 (Figure 3, Figure S3, Table 1) contains 19 grains. It yields Sr/Y values between 0.03 and 27 and an LREE content between 60 and 4,347 ppm. The apatites plot in the LM- (9), IM- (5) and HM-field (5) in the discrimination diagram (Figure S2).

Sample N1 contains 44 apatites (Figures 3 and 4h, Table 1). The Sr/Y values are mostly above 0.1 (91%) and the LREE contents are below 1,000 ppm (59%). The K–S test results of the grain geochemistry distribution indicate that this sample was drawn from a similar distribution as the northern slope samples LPF 3, I1, E1 and HFM (p > 5%, Table S1). Apatites are equally abundant in the HM and LM fields (34%), 10 grains (23%) plot in the IM-field and two in the S- and UM-field (5%).

The youngest southern slope sample G1 (Figures 3 and 4i, Table 1) contains apatites with Sr/Y values mostly (97%) above 0.1 and LREE contents below 1,000 ppm (75%). Thirty-three grain (59%) plots in the LM-field and 14 (25%) in the IM-field. The HM-field (14%) and the UM-field (2%) represent only a minority of the apatites.

Due to a low U and/or a high Pb_c content, only 465 (45%) of the analysed apatites provide U-Pb ages with acceptable ages uncertainties (Figure 5, Table 1). Grouped by their source-rock classification (Figure 5), it is apparent that the majority (76%) of the low-grade metamorphic apatites failed the U-Pb age uncertainty threshold. These grains were not datable due to their low U content (range: 0–130 ppm, median: 7 ppm). U-Pb dating of IM-type apatites had a success rate of 36% which is influenced by the low U content (range: 0–180 ppm, median: 24 ppm) and a high Pb_c content. Cenozoic apatites are particularly sensitive to these problems due to the limited time for radiogenic Pb ingrowth and are hence more likely to fail the U-Pb age uncertainty criterion. The U-Pb age distribution of the LM and IM type apatites may thus be potentially

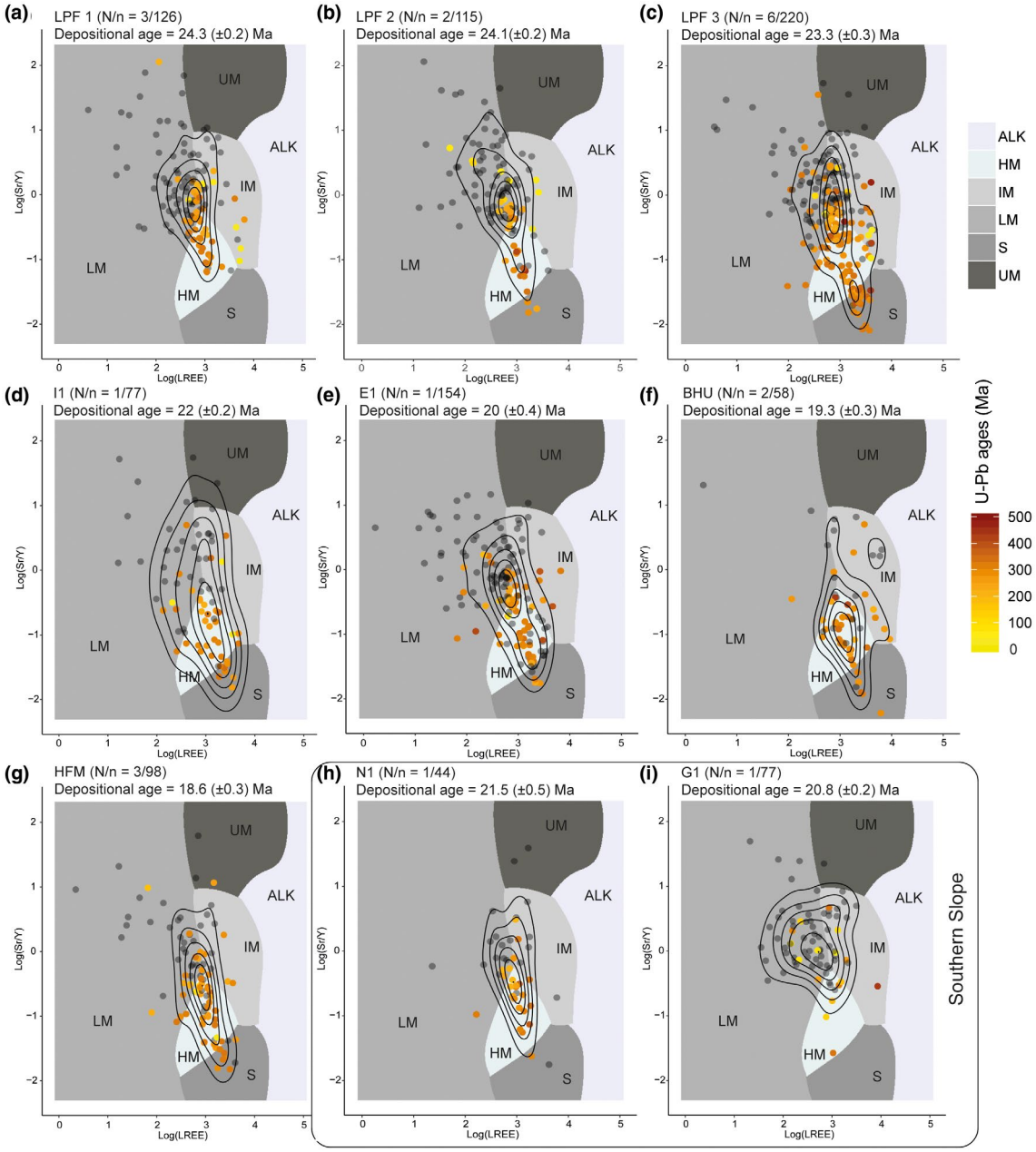

FIGURE 4 Apatite discrimination diagram Log (LREE ppm) versus. Log (Sr/Y) plots after O'Sullivan et al. (2020). Key: IM =mafic I-type granitoids and mafic igneous rocks; LM = low- and medium-grade metamorphic (<upper amphibolite-facies) and metasomatic rocks; HM = partial-melts/leucosomes/high-grade metamorphic rocks; S = S-type granitoids and high aluminium saturation index (>1.1) 'felsic' I-type rocks; UM = ultramafic rocks including carbonatites, lherzolites and pyroxenites. The results of the ATE analysis from the Puchkirchen Trough of the different sample groups are shown (a–j). Black lines in the plots are 2D density contours to visualize the density distribution of each sample. Note the increasing numbers of HM- and S-type apatites in samples from the northern slope (a–g). The younger samples from the southern slope (h and i) contains more grains that plot in the LM field then the older samples. Data points are colour coded by their U-Pb age (see colour bar on the right). Grey points = non-accepted U-Pb age. *N* = number of grouped samples, *n* = number of grains in the group sample. 2σ uncertainties are smaller than the marker size

(but unavoidably) biased by these age uncertainty cut-offs (Chew et al., 2020). In the samples from the northern slope and the HFM, the share of U-Pb ages with acceptable age uncertainties increases from 40% (LPF 1) to 57% (HFM; Figure S4) up-section.

The U-Pb age distribution of apatites with an S-type or HM affinity (85%, 78% accepted ages, respectively) are dominated by grains with Variscan and Permian ages. Apatites that plot in the IM field reveal a number of Alpine ages (20–60 Ma) in addition to the dominant

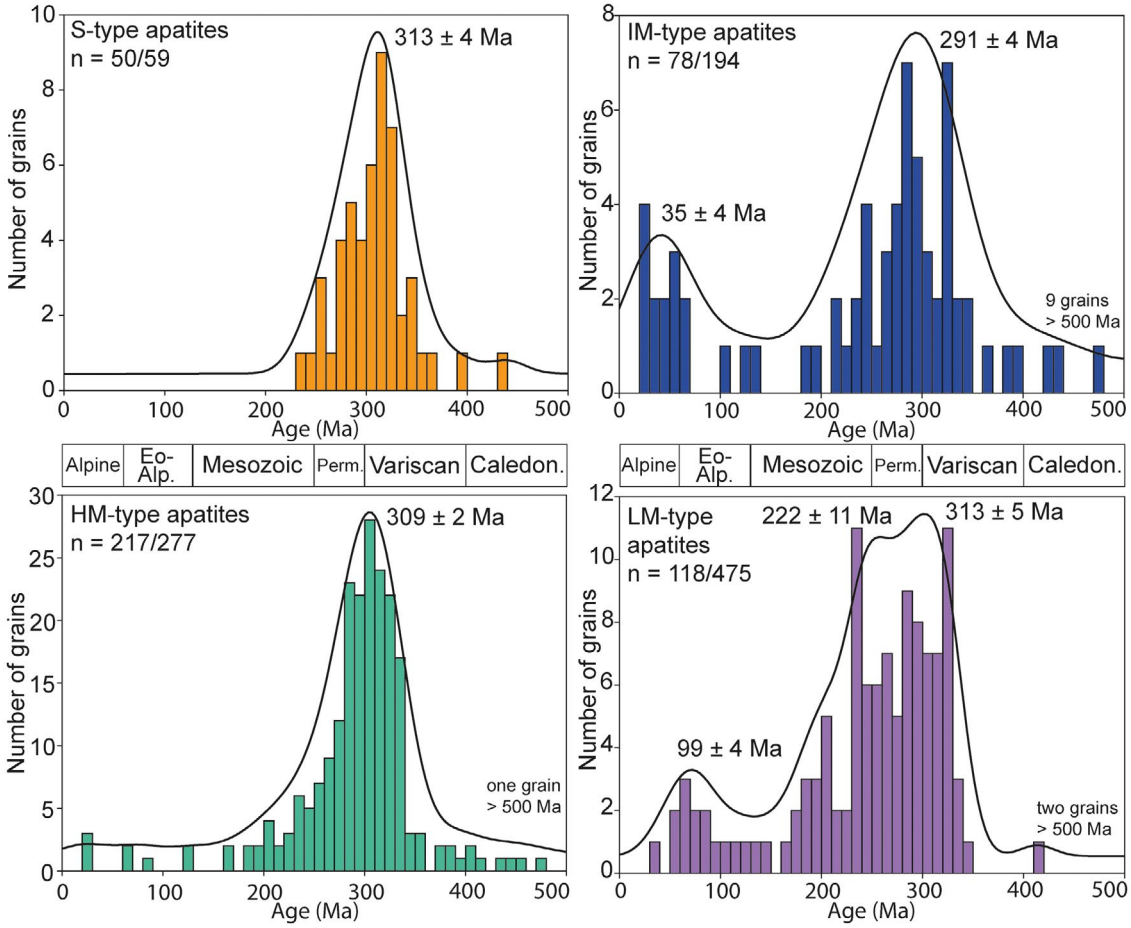

FIGURE 5 Histogram of the apatite U-Pb ages from all samples grouped by their classification are based on the discrimination diagram by O'Sullivan et al. (2020). Note that apatites classified as UM are not shown (17 grains, two successfully dated). Bins of the histogram are 10 Myrs wide; thick black lines are kernel density estimates. Note that the S and HM apatites show a unimodal distribution with a strong late Variscan/Permian peak. The IM and LM apatites both indicate a complex mixture of different age groups with Variscan, Permian, Mesozoic, Eoalpine and Alpine ages. n = n/n is the number of apatites with acceptable U-Pb ages out of the total number of analysed grains

Variscan and Permian ages (Figure 5). U-Pb ages from the low-grade metamorphic apatites (LM) show a number of ages from the Mesozoic (200–130 Ma) and Eoalpine period (130–60 Ma) in addition to a Variscan/Permian age peak (Figure 5).

5.2 | Apatite fission track analysis

Five hundred and seventy-three apatites from 21 samples were dated via the AFT method. All samples and all grouped samples fail the χ^2-test, with the exception of samples T1 and C1 ($P(\chi^2)$ = 0.57, 0.15, respectively; Table 1; Figure S2). The data do not indicate a trend towards younger central ages in the samples from greater depth (Figures S2 and S5). 500–900 m of Upper Austrian NAFB sediments were removed by Late Miocene erosion (Gusterhuber et al., 2012). The basin has a paleo-geothermal gradient of 25°C/km (Gusterhuber et al., 2014). Sample depths vary between 804 and 2,220 m (Table S2). Taken together, the χ^2-test results, the central ages and low geothermal gradient indicate that post-depositional annealing in the basin by burial of the material does not represent a significant source of dispersion in the results, although published AFT length data (12.8–14.6 μm) reveal a mild thermal overprint close to the Alpine front (Brügel et al., 2003; Gusterhuber et al., 2012). Therefore, we interpret our AFT results to reflect orogenic cooling ages.

After the exclusion of grains which have a Periadriatic magmatic source, the AFT results are dominated by Eocene (31%) and Cretaceous ages (31%; Figure 7). Nineteen per cent of the AFT ages are of Oligocene age and 10% of Paleocene age. Miocene (4%) grains and grains older than Cretaceous (7%) represent small age groups.

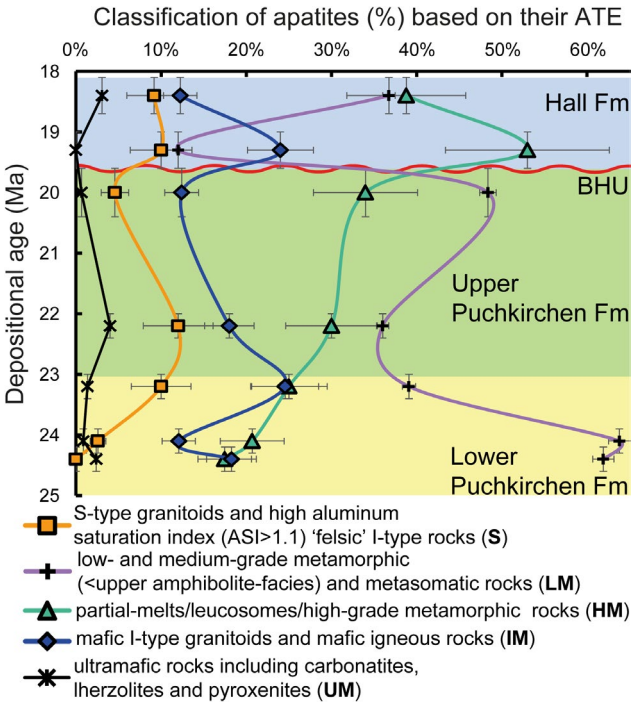

FIGURE 6 Classification of apatites grains from the northern slope samples based on the discrimination diagram of O'Sullivan et al. (2020) plotted against the depositional age of the samples or sample groups. Note the constantly increasing input of HM- and S-field apatites from LPF1 up-section and the corresponding decrease of LM-field apatites (for absolute numbers please see Table 1). Uncertainty bars on the proportion of the different classified apatites represent the proportion of the possibly false classified grains based on the success rate of the discrimination, after O'Sullivan et al. (2020)

Two trends are evident in the samples from the northern slope in the modelled grain-age populations. From sample LPF1 to LPF2, the age of the youngest modelled age peak decreases from 47.0 ± 3.8 Ma (Peak1 [P1]) to 34.9 ± 1.7 Ma (Table 2, Figure 7). In samples LPF3 and I1, this youngest modelled peak is 34.9 ± 2.8 Ma and 36.1 ± 2.1 Ma (Figure 7). The number of Eocene and younger AFT ages increases which leads to an increasing proportion of grains that belong to P1 from LPF2 to I1 (Table 2). Sample E1 contains the youngest modelled AFT grain-age population of 27.5 ± 1.7 Ma (Table 2, Figure 7). This rejuvenation of the modelled grain-age populations leads to a decrease in lag times from LPF1 (22.6 ± 4.0 Ma) to E1 (7.5 ± 2.1 Ma; Figure 8). A similar trend is found in the Variscan and non-Variscan subgroups of the AFT data from LPF 1 (Variscan subgroup: 71.0 ± 11.0 Ma; non-Variscan subgroup: 47.4 ± 3.8 Ma) to E1 (Variscan subgroup: 28.4 ± 2.8 Ma; non-Variscan subgroup: 26.7 ± 2.1 Ma; Table 2). Both subgroups also mirror the decreasing lag-time trend from LPF1 (Variscan subgroup: 46.7 ± 11.2 Ma; non-Variscan subgroup: 23.1 ± 4.0 Ma) to E1 (Variscan subgroup: 8.4 ± 3.2 Ma; non-Variscan subgroup: 6.7 ± 2.5 Ma; Figure 8). The modelled grain-age peaks of the subgroups overlap in these samples within 1σ uncertainty (Table 2).

The BHU sample (Figure 2) contains 42 datable grains; most apatites (82.9 ± 7.1%) are grouped in P1 (46.8 ± 3.1 Ma). The modelled grain-age populations of sample HFM are slightly younger (P1: 39.8 ± 2.6 Ma) than in the BHU sample (Figure 7). The associated

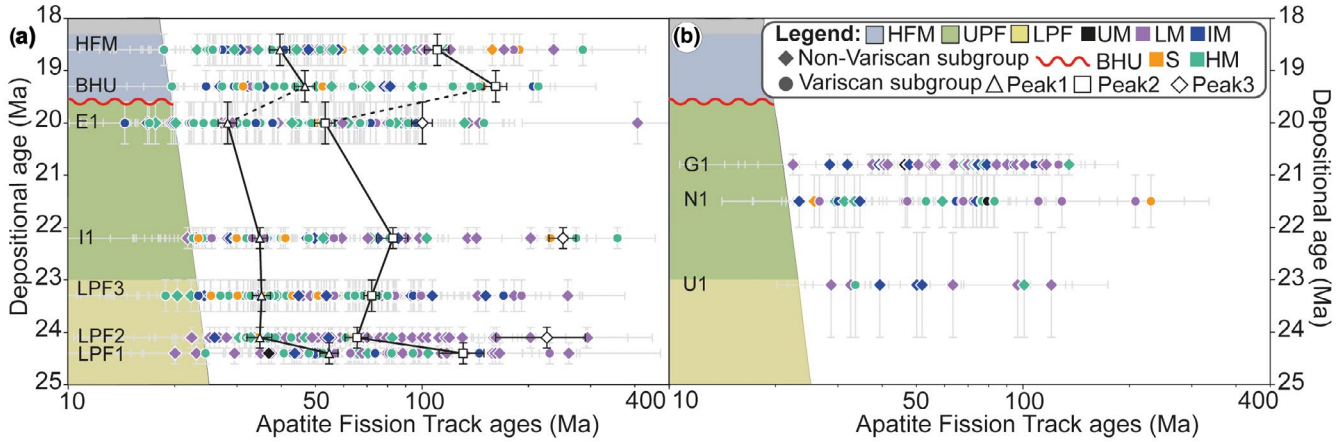

FIGURE 7 Calculated ages (log (Ma)) based on the results of the AFT analyses for the northern (a) and southern (b) slope samples plotted against the depositional age of the (grouped) samples (grains plotting in the IM-field and U-Pb ages between 21 and 60 Ma are excluded). Colours represent the classification of the grains based on the ATE, the marker symbol shows its U-Pb age (Variscan or non-Variscan subgroup). Additionally, the peaks of the grain-age population are plotted in (a). Note the rejuvenation of the modelled grain-age peaks. Uncertainty bars of AFT ages are at the 1σ level. See text for discussion. IM = mafic I-type granitoids and mafic igneous rocks; LM = low- and medium-grade metamorphic (<upper amphibolite-facies) and metasomatic rocks; HM = partial-melts/leucosomes/high-grade metamorphic rocks; S = S-type granitoids and high aluminium saturation index (>1.1) 'felsic' I-type rocks; UM = ultramafic rocks including carbonatites, lherzolites and pyroxenites

TABLE 2 Modelled grain-age populations of the AFT ages from the northern slope (group) samples (P1, P2, P3), their standard deviation (P1 *SD*, P2 *SD*, P3 *SD*) and the proportion of grains that belong to these peaks (F1, F2, F3) within standard deviation (F1 *SD*, F2 *SD*, F3 *SD*)

Sample	Number of grains	P1 (Ma)	P1 *SD* (Ma)	P2 (Ma)	P2 *SD* (Ma)	P3 (Ma)	P3 *SD* (Ma)	F1 (%)	F1 *SD* (%)	F2 (%)	F2 *SD* (%)	F3 (%)	F3 *SD* (%)
LPF1													
All grains	61	47.0	3.8	78.5	7.2	—	—	44.0	13.0	48.0	13.0	—	—
Variscan subgroup	14	71.0	11.0	—	—	—	—	100.0	—	—	—	—	—
Non-Variscan subgroup	47	47.4	3.8	87.5	8.2	—	—	50.0	14.0	50.0	14.0	—	—
LPF2													
All grains	63	34.9	2.8	65.5	4.9	227.0	64.0	35.0	11.0	58.0	11.0	6.0	16.0
Variscan subgroup	8	41.2	2.9	—	—	—	—	100.0	—	—	—	—	—
Non-Variscan subgroup	55	46.5	2.9	124.0	18.0	—	—	72.4	8.9	27.6	8.9	—	—
LPF3													
All grains	95	36.1	2.1	72.3	3.6	—	—	42.5	7.6	57.5	7.6	—	—
Variscan subgroup	46	34.8	2.4	75.4	5.8	—	—	59.0	10.0	41.0	10.0	—	—
Non-Variscan subgroup	49	38.6	3.4	71.6	4.9	—	—	29.1	9.6	70.9	9.6		
I1													
All grains	55	35.0	1.7	83.1	8.3	251.0	22.0	65.7	7.8	24.7	7.6	10.0	11.0
Variscan subgroup	24	35.1	1.9	256.0	22.0	—	—	83.3	7.6	16.7	7.6	—	—
Non-Variscan subgroup	31	37.6	3.2	86.1	8.9	—	—	54.0	12.0	46.0	12.0	—	—
E1													
All grains	103	27.5	1.7	51	3.1	97.6	6.3	37.1	7.8	43.3	8.6	20.0	12.0
Variscan subgroup	34	28.4	2.8	54.4	3.4	101.0	11.0	34.0	11.0	54.0	12.0	13.0	16.0
Non-Variscan subgroup	69	26.7	2.1	46.5	4.5	100.7	7.6	32.0	12.0	44.0	13.0	24.0	17.0
BHU													
All grains	42	46.8	3.1	162.0	12.0	—	—	82.9	7.1	17.1	7.1	—	—
Variscan subgroup	23	38.9	3.3	163.0	12.0	—	—	72.8	9.9	27.2	9.9	—	—
Non-Variscan subgroup	19	59.1	5.3	—	—	—	—	100.0	—	—	—	—	—
HFM													
All grains	68	39.8	2.6	110.6	8.8	—	—	68.4	8.1	39.8	2.6	—	—
Variscan subgroup	30	35.3	2.6	117.7	9.6	—	—	69.8	9.0	117.7	9.6	—	—
Non-Variscan subgroup	38	55.6	4.1	—	—	—	—	100.0	—	—	—	—	—

lag times of P1 are between 27.5 ± 3.4 Ma (BHU) and 21.2 ± 2.9 Ma (HFM, Figure 8). In these two samples, the AFT age peaks of the two subgroups (Variscan and non-Variscan) do not overlap within their 1σ uncertainty (Table 2, Figure 8).

Due to the small number of analysed apatites (81) and samples (three) from the southern slope, a clear trend is not detectable. In the older samples U1 and N1 (Figures 2 and 7), grains with Oligocene, Eocene, Paleogene and Cretaceous ages are present. In the younger sample G1 (Figure 2), mostly Eocene, Paleocene and Cretaceous ages are present. Only three grains are younger than the Eocene.

6 | DISCUSSION

6.1 | Provenance of detrital apatites

6.1.1 | Samples from the northern slope and the HFM

The increasing abundances of apatites with high LREE and lower Sr/Y values in the samples from the northern slope and the HFM (Figure 6) are interpreted as reflecting increasing input from high-grade (≥upper amphibolite-facies) metamorphic sources. Consistent with this interpretation, the amount of acceptable U-Pb ages increases

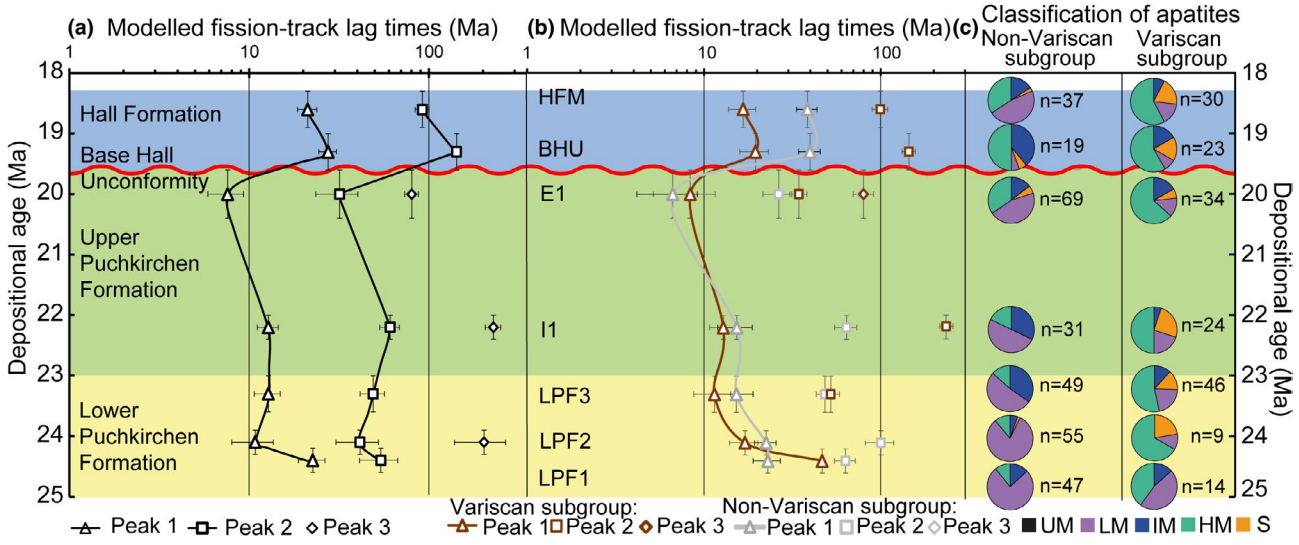

FIGURE 8 (a) Lag times of modelled peak ages of the AFT grain-age population (log (Ma)) of the samples from the northern slope. (b) Lag times of modelled peak ages of the two subgroups (Variscan, non-Variscan subgroup) of the samples. (c) Classification of the apatites belonging to the subgroups and number of grains (*n*) in the subgroup for every sample. Note that the lag-time Peak1 of both subgroups overlap during the samples LPF2, LPF3, I1 and E1 within 1σ uncertainty. We interpreted this as indicating a similar thermal history for both groups. Both subgroups differ in the HFM sample group in their modelled lag-time peaks. We attributed this to an input from a different source with longer lag times in the non-Variscan subgroup, probably the AFM. Note the small number of apatites in the BHU sample group what hampers interpretation. See text for discussion. IM = mafic I-type granitoids and mafic igneous rocks; LM = low- and medium-grade metamorphic (<upper amphibolite-facies) and metasomatic rocks; HM = partial-melts/leucosomes/high-grade metamorphic rocks; S = S-type granitoids and high aluminum saturation index (>1.1) 'felsic' I-type rocks; UM = ultramafic rocks including carbonatites, lherzolites and pyroxenites

from LPF1 (40%) to HFM (58%, Figure S4), as high-grade metamorphic apatites are more suitable for U-Pb dating than low-grade metamorphic apatites due to their higher U contents (Henrichs et al., 2018).

Similarly, Sharman et al. (2018) found a change in the detrital zircon U-Pb age distribution from the LPF to UPF, indicated by a decreasing number of zircons with ages >525 Ma and an increase in ages between 250 and 375 Ma. These authors interpret their results to reflect increasing longitudinal sediment bypass from the German NAFB (Figure 1), as a result of the development of the Halfinger Canyon in early Aquitanian times on the shelf close to Munich (Figure 3). Concurrently, transverse sediment delivery from the Eastern Alps in the south via the AFM decreased. However, increased sediment bypass from the Munich shelf cannot explain our results for two reasons. (a) The Halfinger Canyon cuts into Lower Aquitanian Marls on the shelf (Zweigel, 1998). Therefore, the Halfinger Canyon must have been established well after the Chattian/Aquitanian boundary (23.0 Ma) and after the recorded change towards a source with abundant high-grade metamorphic apatite at 23.3 (±0.3) Ma (Figures 3 and 6). (b) The sediment-routing system in the Upper Austrian NAFB experienced a major rearrangement at 19.0 Ma. Eastward-directed, channel-controlled sediment transport ended and clinoforms started to prograde northward into the basin (Figure 3; Hülscher et al., 2019), leading to a cut-off of sediment supply from the NAFB west of Munich (Kuhlemann & Kempf, 2002). Our ATE and U-Pb results suggest that the apatite provenance has not changed from sample group LPF3 to the HFM (Figure 6). The sources of the high-grade (≥upper amphibolite-facies) metamorphic apatites with late Variscan/Permian U-Pb ages (Figure 5) must still have been connected to the Upper Austrian NAFB.

For the above reasons, we regard the Munich delta system as a subordinate apatite source for the Upper Austrian NAFB – except for the BHU samples, see below – and interpret the increasing abundances of late Variscan/Permian, high-grade metamorphic apatites to be linked to processes in the Eastern Alps and the paleo-Inn drainage network. A comparison with thermochronological results from pebbles from the Chiemgau and Wachtberg paleo-Inn fans shed from the Eastern Alps reveals a similar age range (Variscan, Permian, Eoalpine, and Alpine K-Ar ages, Oligocene to Cretaceous AFT ages; Brügel et al., 2003) as found in our northern slope samples by the U-Pb and AFT thermochronometers (Figure 7, Figure S3). Additionally, we found a similar rejuvenation trend in our AFT grain-age populations as described from the late Oligocene to early Miocene deposits of the paleo-Inn (Figures 1 and 9; Dunkl et al., 2009; Kuhlemann et al., 2006). Based on

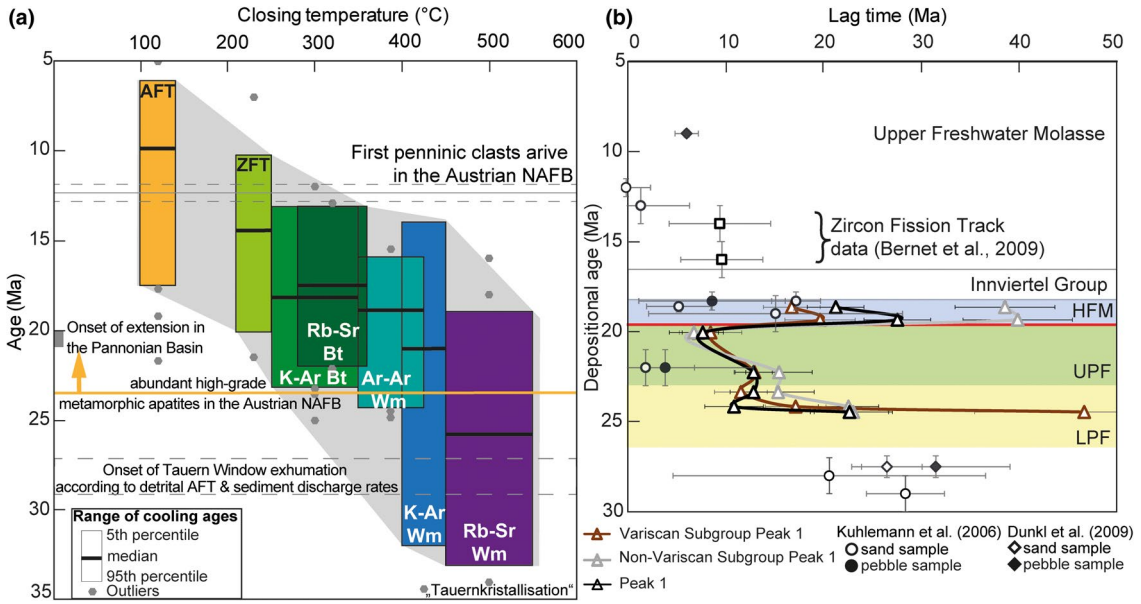

FIGURE 9 Comparison between thermochronological data from the Tauern Window (a) and from the sedimentary deposits in the NAFB (b). In (b) only the youngest modelled peaks are shown; note that in the 27.5 Ma old sand sample from Dunkl et al. [2009], the youngest modelled age peak was excluded because the authors interpreted it to be derived from the Periadriatic magmatic chain. For literature sample location of (a), see Figure S6 and (b), see Figure 1. The depositional ages and their uncertainties were partly recalibrated to the updated basin stratigraphy. Cooling ages in (a) are from the Penninic and Subpenninic units of the Tauern Window and mirror the cooling following the Barrovian-peak metamorphism ("Tauernkristallisation") of these units. Light grey area represents the range of regionally variable cooling paths realized in the Tauern Window. At 23.3 ± 0.3 Ma, the high-grade metamorphic apatites became abundant in the Upper Austrian NAFB. Cooling of the Tauern Window accelerated at 23–21 Ma with the onset of tectonic activity along orogen-perpendicular normal faults at the eastern and western end of the window. At 13 Ma, the window reached the surface as documented by Penninic pebbles observed in the Austrian MKH fans (Brügel et al., 2003). The cooling trend in the Tauern Window (a) is in line with the AFT data from the sedimentary record (b) in the foreland. AFT lag-times decrease from 20–30 Ma in samples older than 24.1 Ma to 2–12 Ma thereafter. In Upper Freshwater Molasse sediments, Bernet et al. (2009) found zircon fission track ages with lag-times <10 Ma. Data from (a): Bertrand et al., 2017; Blanckenburg et al., 1989; Borsi, 1978; Cliff et al., 1985; Dunkl et al., 2003; Favaro et al., 2015; Foeken et al., 2007; Fügenschuh et al., 1997; Grundmann & Morteani, 1985; Hawkesworth, 1976; Inger & Cliff, 1994; Jäger et al., 1969; Lambert, 1970; Most, 2003; Oxburgh et al., 1966; Raith et al., 1978; Reddy et al., 1993; Roddick et al., 1980; Satir, 1976; Satir & Morteani, 1982; Scharf, Handy, Favaro, et al., 2013; Staufenberg, 1987. Closure temperatures: Rb-Sr White Mica: 500 ± 50°C (Purdy & Jäger, 1976); K-Ar White Mica: 425 ± 50°C (Blanckenburg et al., 1989); Ar-Ar White Mica: 387.5 ± 37.5°C (Reiners & Brandon, 2006); K-Ar Biotite: 320 ± 40°C (Del Moro et al., 1982); Rb-Sr Biotite: 300 ± 50°C (Jäger, 1967); Zircon Fission Track: 230 ± 20°C (Reiners & Brandon, 2006); Apatite Fission Track: 120 ± 20°C (Reiners & Brandon, 2006)

these similarities, we interpret the apatites in the northern slope samples to have been sourced dominantly by longitudinal sediment delivery from the proximal Wachtberg and Chiemgau fans. However, a transverse component is noticeable by the continuous appearance of pre-Tertiary AFT ages (Figure 7, Figure S2) which are a minority in 22 Ma paleo-Inn deposits but common in the AFM (Frisch et al., 2001; Kuhlemann et al., 2006).

Potential source rocks for the HM- and S-field apatites in the Eastern Alps are portions of the Ötztal-Bundschuh nappe system (Figure 1). The Ötztal-Stubai nappe complex underwent upper amphibolite-to-eclogite-facies conditions (6–15 kbar, 550–700°C) during the Variscan orogeny but did not experience any Permo-Mesozoic or high-grade (≥upper amphibolite-facies) Eoalpine metamorphic imprint (Miller & Thöni, 1995; Rode et al., 2012; Schulz et al., 2019). This is in accordance with the observed U-Pb grain-age distribution of the high-grade metamorphic apatites (Figure 5).

LM affinity apatites partly show Permo-Mesozoic U-Pb ages, which implies in parts of the source a metamorphic overprint of this age (Figure 5). The source might have been the Drauzug-Gurktal nappe system, as these nappes were affected by the Variscan orogeny and recorded a subsequent upper greenschist-/lower amphibolite-facies (2.4–4.2 kbar, 450–530°C), Permo-Mesozoic metamorphic event (Schuster et al., 2001, 2015). These nappes structurally overlie the Ötztal-Bundschuh nappes but did not experience an Eoalpine overprint (Schmid et al., 2004). The appearance of apatite U-Pb ages between 21 and 60 Ma that plot in the IM-field (Figure 5) shows that the Eocene/Oligocene (zircon U-Pb ages: 43–24 Ma; Ji et al., 2019)

intrusions along the Periadriatic Line were part of the paleo-Inn drainage network (Brügel et al., 2000; Sharman et al., 2018). However, these interpretations might be partly biased by the high number of apatites of IM (64%) and LM (76%) affinity which failed the U-Pb age uncertainty threshold filter.

Sample group BHU is enriched in LREE-rich apatites with long AFT lag times compared to all other northern slope samples (Figures 4 and 7). This period of channel sedimentation is characterized by an erosional period on the shelf close to Munich (Zweigel, 1998) and the remobilization of shelf strata into the Puchkirchen channel system (Grunert et al., 2013). This remobilized shelf sediment is a potential source of the apatites in the BHU sample, but the interpretation is complicated by the small sample size (58 grains, Table 1).

In the HFM sample group, the fraction of apatites plotting in the HM- and S-field reaches a maximum (Figures 4 and 6). The youngest modelled AFT age peak (P1: 39.8 ± 2.6 Ma) is older compared to sample E1 in the UPF, even though several rapidly cooled apatites were found (Figures 7 and 8, Figure S2). This increase in age is in contrast with previously published modelled AFT age peaks (P1: 23.8 ± 3.0 Ma, 26.9 ± 7.0 Ma; Kuhlemann et al., 2006; Figure 9) from the proximal Wachtberg Fan (Figure 1). The Upper Marine Molasse is characterized by strong tidal currents (Grunert et al., 2012), which could have mixed our distal HFM sample more efficiently with redeposited material from the AFM (see below) than the proximal samples of Kuhlemann et al. (2006), resulting in the observed increase in AFT ages. This interpretation is supported by the differences between the modelled AFT age peaks of the Variscan and non-Variscan subgroups in the BHU and HFM sample groups (Figure 8), pointing to a different thermochronological evolution of the source areas of the two subgroups. The younger AFT ages (Variscan subgroup) may be derived directly from the exhuming hinterland, whereas the older AFT ages (non-Variscan subgroup) may be redeposited from the AFM. Detrital AFT ages from southern Alpine foreland deposits of Burdigalian age show a young (22.2 ± 2.4 Ma, 17.7 ± 5.5 Ma) modelled age peak (Stefani et al., 2007; Zattin et al., 2003). These young grains may reflect a northward migration of the drainage divide into the area of the future Tauern Window (Figure 10), an interpretation which is challenged by the constant sandstone petrography of southern Alpine foreland sediments (Stefani et al., 2007). Nevertheless, we interpret the mixing of a young and older AFT signal in the Upper Austrian NAFB and a northward migration of the drainage divide to be the origin of the differences between the AFT age peaks of Kuhlemann et al. (2006) and our dataset (Figure 9).

6.1.2 | Samples from the southern slope

Samples U1 and N1 from the southern slope (Figure 4, Figure S3) show similar U-Pb age, ATE and AFT data as the samples LPF3, I1, E1 and HFM and probably reflect a similar provenance. In the G1 sample, the presence of Eoalpine U-Pb ages (Figure 4, Figure S4) shows that the grains were likely sourced from the Koralpe-Wölz nappe system which experienced Eoalpine metamorphism (Figure 1) (Krenn et al., 2012; Thöni & Miller, 2000). We interpret the differences in AFT, ATE and U-Pb data (Figures 4 and 7, Figure S4, Table 1) between samples G1 and N1 to be related to the redeposition of the AFM south of the Upper Austrian NAFB (Figure 1). The interpretation is supported by the similar AFT grain-age distribution of sample G1 (Figure 7 and Figure S2) and the AFM (Frisch et al., 2001). Reworking started between the deposition of sample N1 (21.5 ± 0.5 Ma) and sample G1 (20.8 ± 0.2 Ma), which is in line with previous estimates of ca. 21 Ma (Frisch et al., 2001). In early Miocene times (23–21 Ma), the drainage network of the AFM must have reached back to the magmatic complexes close to the Periadriatic Line (34–28 Ma; Borsi et al., 1979) due to the appearance of apatites (Figure S3) and zircons (Sharman et al., 2018) with Alpine U-Pb ages on the southern slope and volcanic material in the formation itself (Frisch et al., 2001).

6.2 | Thermochronological evolution of the Eastern Alps from 29 to 18 Ma

The detrital AFT results reveal that in late Oligocene/early Miocene times the Eastern Alps were in large parts a slowly (<0.1 mm/a) exhuming mountain range, as suggested by previous studies (Frisch et al., 1998; Kuhlemann, 2007). Most (77%) AFT single-grain ages are older than the Oligocene (>33.9 Ma) and have lag times >10 Ma (Figures 7 and 8). Our AFT results are dominated by the Paleocene to Eocene cooling of the Austroalpine units following the Eoalpine orogeny and only to a lesser extent record processes that started after the Alpine continent-continent collision at 35 Ma (Handy et al., 2010).

However, starting from sample group LPF2, an increasing number of fast-cooled AFT ages (lag times <10 Ma) appear in the northern slope samples, an up-section trend which cumulates in a minimum lag time of 7.5 ± 2.1 Ma at 20 Ma (Figure 8, Table 2). In combination with the change towards a higher abundance of high-grade metamorphic apatites in these samples, the decreasing lag times on the northern slope suggest accelerated exhumation in the Eastern Alps (Figure 10). This acceleration started around

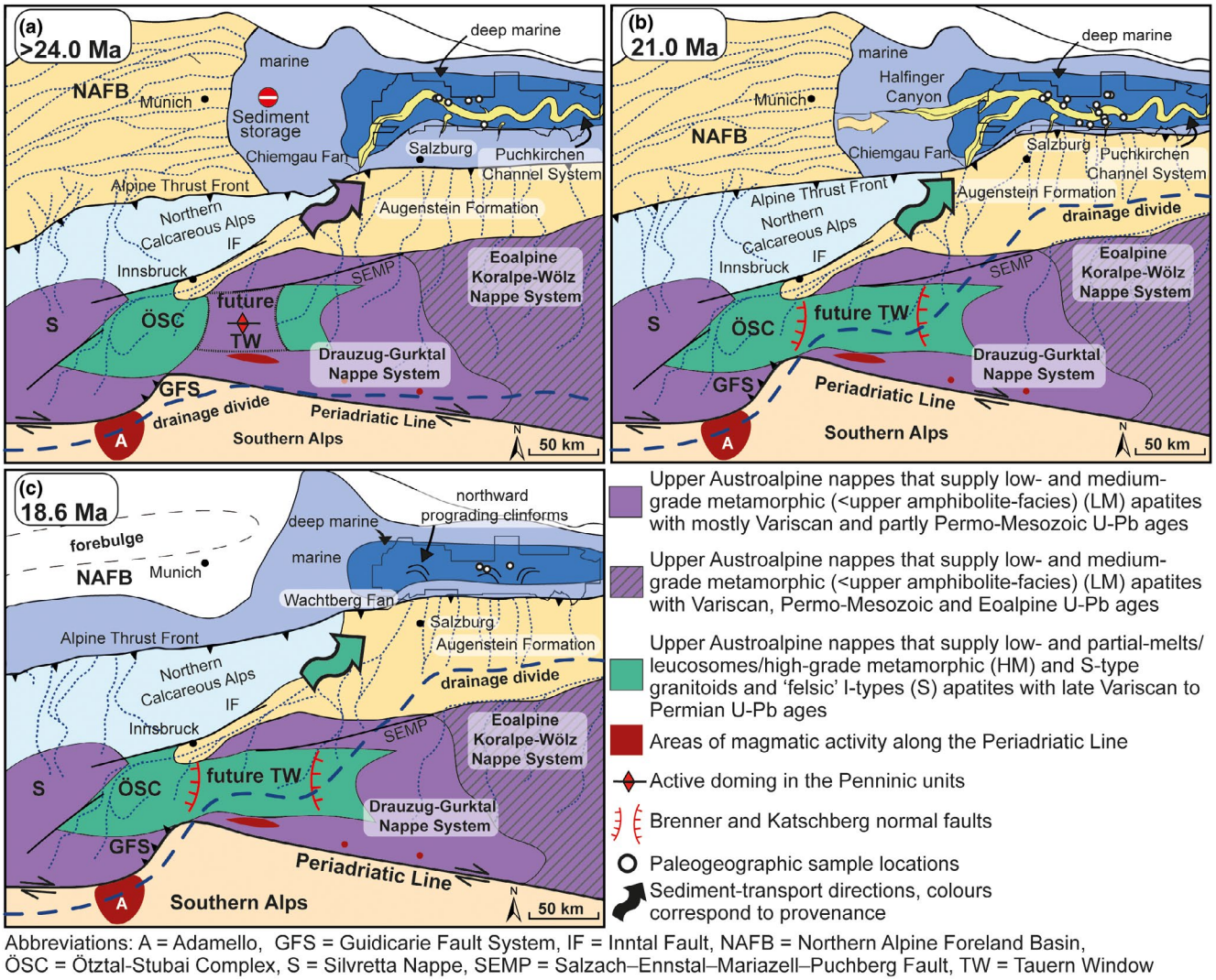

FIGURE 10 Paleogeographic reconstructions of the eastern NAFB and the Eastern Alps before 24 Ma (a), around 21 Ma (b) and around 18.6 Ma (c), redrawn after Sharman et al. (2018), Kuhlemann and Kempf (2002), Frisch et al. (1998), and Ortner and Stingl (2001). Before 24 Ma (a), the Upper Austroalpine units of the Eastern Alps shed apatites with low-grade metamorphic trace-element geochemistry and a Permo-Mesozoic U-Pb age peak onto the northern slope of the Upper Austrian NAFB. Upper Austroalpine units above the future Tauern Window experienced enhanced exhumation due to the active doming of the underlying Penninic units of the future Tauern Window. The AFM was deposited on top of the present day Northern Calcareous Alps (Frisch et al., 2001). The drainage divide (blue, dashed line) was located close to the Periadriatic Line. The shelf around Munich trapped the sand-sized sediment from the west (Sharman et al., 2018). From 23.3 ± 0.3 Ma onward (b), the apatite single-grain distribution in the northern slope samples became dominated by grains from high-grade metamorphic source-rocks and Variscan/Permian U-Pb ages above the future Tauern Window, which are the sources of the fast-cooled apatites. On the Munich shelf, the Halfinger Canyon developed after 23.0 Ma (Zweigel, 1998) but represented a subordinate sediment source for the Puchkirchen Channel System. The drainage divide (blue, dashed line) was still located in the Adamello area but moved east of it, northwards into the area of the future Tauern Window, as revealed by young AFT ages in the Southern Alpine Foreland Basin (Stefani et al., 2007; Zattin et al., 2003). The AFM was uplifted and redeposited from 21 Ma onward. At 19.0 Ma (c), channel sedimentation ended in the Upper Austrian NAFB and clinoforms prograded northward. The NAFB west of Munich was cut-off from the Upper Austrian NAFB as sediment source. Sample positions relative to the channel may differ from the description in Table 1 due to the lateral variability of the channel through time

27.5 ± 1.7 Ma as revealed by the AFT ages in sample E1 (Figure 8) and by AFT gneiss pebble data from 22 Ma old Chiemgau Fan deposits (30.9 ± 2.0 Ma, 25.8 ± 8.0 Ma; Figure 9; Brügel et al., 2003; Kuhlemann et al., 2006). Both AFT subgroups (Variscan and non-Variscan U-Pb ages) were affected by this, as they both show a similar lag-time evolution (Figure 8). AFT lag times could have been shortened by a thermal perturbation due to magmatic activity along the Periadriatic Line as suggested by Kuhlemann et al. (2006). However, this interpretation is challenged

by the >50 Ma old zircon fission track ages of pebbles from the Chiemgau Fan (Brügel, 1998) and the increasing abundance of high-grade metamorphic apatites at 23.3 Ma in our samples (Figure 6). Both findings cannot be explained by a thermal perturbation along the Periadriatic Line. Our interpretation of accelerated exhumation after 27.5 ± 1.7 Ma is supported by the doubling of Eastern Alpine sediment-discharge rates from 1,072 ± 167 km^3/Myr before 29 Ma to 2,486 ± 375 km^3/Myr after 29 until 21 Ma (values represent the arithmetical mean and the standard deviation of the discharge rates from the Eastern Alps to all circum-Alpine basins during the time period; Kuhlemann et al., 2001). The increase in exhumation rates cannot be associated with a change in climate (e.g. higher precipitation rates) as global (Cramer et al., 2009) and regional (Mosbrugger et al., 2005) climate proxies suggest stable climatic conditions. The exhumation (constrained to ca. 29 Ma by the sediment-discharge rates [Kuhlemann et al., 2001] and ca. 27 Ma by the AFT data) was thus tectonically triggered (Rosenberg & Berger, 2009).

We interpret these observations to reflect an early exhumation period of the Tauern Window. After the end of oceanic subduction in the Eastern Alps, the accretion of European crust at the base of the Adriatic plate culminated in subsequent Barrovian metamorphism in the thickened crust (Schmid et al., 2013). Peak metamorphic temperatures were variable in space and reached up to 600°C in the centres of the two Tauern subdomes (Figure 1) (Bousquet et al., 2012; Groß et al., 2021). Estimates for the timing of peak metamorphism range from 40–30 Ma (Christensen et al., 1994; Favaro et al., 2015; Glodny et al., 2005; Grundmann & Morteani, 1985; Ratschbacher et al., 2004; Schneider et al., 2015; Selverstone, 1988; Zimmermann et al., 1994) to ca. 20 Ma, depending on the region and structural level exposed (Blanckenburg et al., 1989). Ongoing upper and lower plate convergence was translated into shortening localized in the Tauern Window region in the form of large-scale upright folding (Figure 10). This is recorded by concentric cooling age patterns, with the youngest ages in the centres of the antiformal dome structures of the window (Reddy et al., 1993; Scharf, Handy, Ziemann, et al., 2013; Schneider et al., 2015). Folding led to the onset of early Oligocene (30–28 Ma) vertical rock uplift and resultant exhumation and cooling of the Tauern Window, as witnessed by the earliest cooling ages (U-Pb on apatite, Rb-Sr on white mica) postdating accretion of European crust and the climax of regional metamorphism (Favaro et al., 2015; Schneider et al., 2015). The overlying Upper Austroalpine nappes responded to this upright folding with focused erosional denudation as witnessed by the increasing number of high-grade metamorphic apatites and decreasing AFT lag times in our dataset (Figure 9). Spatially restricted but fast eroding areas with a high mineral fertility can dominate the single-grain distributions of orogen-wide sediment-routing systems (Malusà et al., 2017). Our inferred onset of this exhumation at 29–27 Ma is in line with the onset of cooling in the Tauern Window (31–28 Ma; Favaro et al., 2015; Reddy et al., 1993; Schneider et al., 2015).

Based on the doubling of the sediment-discharge rates after 29 Ma, we assume that 11,308 ± 4,334 km^3 more material was eroded from the Eastern Alps between 29 and 21 Ma (2,486 ± 375 km^3/Myr) than between 34 and 29 Ma (1,072 ± 167 km^3/Myr) (Kuhlemann et al., 2001). By dividing this additional amount of material through the area above the future Tauern Window (3,125 km^2; Favaro et al., 2017), these two estimates suggest that a 3.6 ± 1.4 km thick rock unit was eroded during the early exhumation period from 29 to 21 Ma. This fits in with estimates from the AFT results presented here, which imply erosion of a ca. 3.3–4.7 km thick rock unit of Upper Austroalpine Nappe provenance in the Eastern Alps from 29–27 to 20 Ma.

6.3 | Trigger of early and slow exhumation of the Tauern Window

Southern Alpine indentation is the most likely driver of the early Tauern Window exhumation, which was focused in a fairly restricted area of the central Eastern Alps. Lateral escape of the Eastern Alps and retreat of the Pannonian slab both started later, at respectively 23–21 Ma (Horváth et al., 2006) and during the Late Neogene (Linzer et al., 1998), and can be excluded as the trigger for early exhumation of the Tauern Window. Indentation of the Southern Alps has been suggested as a driver for the Tauern Window exhumation by several authors (Ratschbacher et al., 1991; Rosenberg et al., 2007; Royden, 1988; Scharf, Handy, Favaro, et al., 2013). The main, rapid period of this indentation started around 23–21 Ma (Pomella et al., 2011, 2012); however, Favaro et al. (2015) inferred that early Adriatic indentation began around 28 Ma. At this stage, early strike-slip faulting has been recognized along the Inntal fault system (Ortner et al., 2006), the Defereggen-Antholz-Vals fault (Müller et al., 2000) and the Salzach–Ennstal–Mariazell–Puchberg fault (Figure 1; Rosenberg & Schneider, 2008; Schneider et al., 2013).

Contemporaneously at 32–28 Ma, mylonitic and brittle E-W directed transpression (Figure 1) as well as syn-tectonic magmatism testifies to motion along the Giudicarie Fault System (GFS; Figures 1 and 10) southwest of the Tauern Window (Martin et al., 1993; Müller et al., 2001; Prosser, 1998). Adriatic indentation into the Eastern Alps along the GFS can explain why exhumation was localized in the Tauern Window region. This is

evident by the large (≥20 km) amount of exhumation that took place northeast of the GFS (Favaro et al., 2017). In contrast, the Adriatic indenter itself is largely unaffected by exhumation (Rosenberg et al., 2018) and Austroalpine units NW of the GFS experienced only a small (10–12 km) degree of collisional shortening (Rosenberg & Kissling, 2013). This early indentation must have started at the latest by 28 Ma, as suggested by the earliest cooling ages in the Tauern Window (Favaro et al., 2015; Reddy et al., 1993; Schneider et al., 2015) and the AFT data presented here, and lasted until 23–21 Ma (Favaro et al., 2015). According to the AFT cooling ages presented in this study, exhumation in response to indentation from 29–27 Ma to 20 Ma caused 3.3–4.7 km of erosional denudation (0.3–0.6 mm/a) and reflects slower exhumation than in the period from 21 to 13 Ma, when the rates increased to 1.5–2 mm/a (Frisch et al., 2000).

The increased indentation (Verwater et al., 2021) and exhumation rates after 21 Ma (Frisch et al., 2000) are associated with a transition from exhumation dominated by orogen-perpendicular shortening to orogen-parallel extension (Favaro et al., 2017) via normal faults localized at the eastern and western ends of the Tauern Window (Behrmann, 1988; Frisch et al., 2000; Fügenschuh et al., 1997; Genser & Neubauer, 1989; Scharf, Handy, Favaro, et al., 2013; Selverstone, 1988). Estimates of the amount of orogen-parallel extension along those faults are debated and range between 14 and 160 km (Favaro et al., 2017; Frisch et al., 2000; Fügenschuh et al., 2012; Linzer et al., 2002; Rosenberg & Garcia, 2011; Scharf, Handy, Favaro, et al., 2013; Wolff et al., 2020). The transition was caused by modifications of the boundary conditions of the orogen, namely the opening of the Pannonian basin in the east at 21 Ma (Horváth et al., 2006) and the cessation of the propagation of the northern Alpine front around the same time (Hinsch, 2013; Ortner et al., 2015). Adriatic motion was no longer transferred into propagation of the northern Alpine front (Figure 10), but mainly into indentation along the GFS (Pomella et al., 2011, 2012; Prosser, 1998, 2000) and eastward lateral escape of the Eastern Alps (Ratschbacher et al., 1991).

7 | CONCLUSIONS

In this paper, we reconstruct the early exhumation (from 29 to 27 Ma onward) of the Tauern Window in the central European Eastern Alps by combining geochemical (trace-element geochemistry) and thermochronological (U-Pb, FT) single-grain analysis on detrital apatites from Oligocene/Miocene sediments of the Upper Austrian NAFB. This highly discriminative single-grain multi-proxy approach reveals three major trends from the Oligocene samples up-section into the earlier Miocene: (1) an increasing proportion of grains from a high-grade metamorphic source with late Variscan/Permian U-Pb ages, (2) an increase in U-Pb ages with acceptable age uncertainties, and (3) an increasing number of Oligocene AFT ages.

When integrated with previously published results from single-grain and pebble analysis of paleo-Inn river deposits in the eastern NAFB, we show that the majority of the apatites in the Upper Austrian NAFB were delivered from the Eastern Alps. Furthermore, our and previously published data suggest an exhumation event in the Eastern Alps starting at 29–27 Ma that we attribute to the surface response to the onset of upright folding and doming in the Penninic units of the future Tauern Window in front of the Adriatic indenter. Data from the presently exposed Penninic units of the Tauern Window support the interpretation of an early period of doming-related exhumation starting at 31–28 Ma (Favaro et al., 2015; Reddy et al., 1993; Schneider et al., 2015). Early Adriatic indentation documented by motion along the Giudicarie Fault System (Martin et al., 1993; Müller et al., 2001; Pomella et al., 2011) drove this early and slow (0.3–0.6 mm/a) exhumation period from 29–27 to 23–21 Ma which removed 3.3–4.7 km of rocks of Upper Austroalpine units above the future Tauern Window.

ACKNOWLEDGEMENTS

We thank RAG Austria AG for providing the 3D seismic-reflection data set and access to the samples. Schlumberger is acknowledged for the donation of the Petrel license. We especially thank Ewald Hejl for providing the samples H1, Z1, A1 and F1, and Jan Pleuger and Mark Handy (both FU Berlin) for comments on this work. AB and ES acknowledged funding by the DFG (grants BE 5070/ 7-1 and SO 436/ 16-1). DC acknowledges support by a research grant from Science Foundation Ireland under Grant Number 13/RC/2092 and 13/RC/2092_P2, which is co-funded under the European Regional Development Fund and by PIPCO RSG and its member companies. Open access funding enabled and organized by Projekt DEAL. We thank two anonymous reviewers, Susanne Schneider and editor Kerry Gallagher for their critical and careful treatment of the manuscript.

AUTHORS CONTRIBUTIONS

JH, VV and PG wrote the manuscript with major contributions by DC, ES and AB. JH drew all figures, took the samples, undertook interpretation of the seismic-reflection data and conducted the AFT analysis under the supervision of ES, who helped during sample preparation. DC helped with the ATE and U-Pb analysis. AB, ES and JH designed the study. AB provided the funding.

PEER REVIEW

The peer review history for this article is available at https://publons.com/publon/10.1111/bre.12593.

DATA AVAILABILITY STATEMENT

The data that support the findings of this study are available in the supplementary material of this article.

ORCID

Julian Hülscher https://orcid.org/0000-0002-5041-6907
Edward R. Sobel https://orcid.org/0000-0001-5030-8773
Vincent Verwater https://orcid.org/0000-0003-3738-280X
Philip Groß https://orcid.org/0000-0002-5766-169X
David Chew https://orcid.org/0000-0002-6940-1035
Anne Bernhardt https://orcid.org/0000-0002-2584-511X

REFERENCES

Behrmann, J. H. (1988). Crustal-scale extension in a convergent orogen: The Sterzing-Steinach mylomte zone in the Eastern Alps. *Geodinamica Acta*, *2*(2), 63–73.

Belousova, E., Griffin, W., O'Reilly, S., & Fisher, N. (2002). Apatite as an indicator mineral for mineral exploration: Trace-element compositions and their relationship to host rock type. *Journal of Geochemical Exploration*, *76*(1), 45–69.

Belousova, E., Walters, S., Griffin, W., & O'Reilly, S. (2001). Trace-element signatures of apatites in granitoids from the Mt Isa Inlier, northwestern Queensland. *Australian Journal of Earth Sciences*, *48*(4), 603–619.

Bernet, M. (2019). Exhumation studies of mountain belts based on detrital fission-track analysis on sand and sandstones. In M. G. Malusà, & P. G. Fitzgerald (Eds.), *Fission-track thermochronology and its application to geology* (pp. 269–277). Springer.

Bernet, M., Brandon, M., Garver, J., Balestieri, M., Ventura, B., & Zattin, M. (2009). Exhuming the Alps through time: Clues from detrital zircon fission-track thermochronology. *Basin Research*, *21*(6), 781–798.

Bernhardt, A., Stright, L., & Lowe, D. R. (2012). Channelized debris-flow deposits and their impact on turbidity currents: The Puchkirchen axial channel belt in the Austrian Molasse Basin. *Sedimentology*, *59*(7), 2042–2070.

Bertrand, A., Rosenberg, C. L., Rabaute, A., Herman, F., & Fügenschuh, B. (2017). Exhumation mechanisms of the Tauern Window (Eastern Alps) inferred from apatite and zircon fission track thermochronology. *Tectonics*, *36*(2), 207–228.

Blanckenburg, F. V., Villa, I., Baur, H., Morteani, G., & Steiger, R. (1989). Time calibration of a PT-path from the Western Tauern Window, Eastern Alps: The problem of closure temperatures. *Contributions to Mineralogy and Petrology*, *101*(1), 1–11.

Borsi, S. (1978). *New geopetrologic and radiometric data on the Alpine history of the Austridic continental margin south of the Tauern Window (Eastern Alps)*. Società cooperativa tipografica.

Borsi, S., Del Moro, A., Sassi, F., & Zirpoli, G. (1979). On the age of the Vedrette di Ries (Rieserferner) massif and its geodynamic significance. *Geologische Rundschau*, *68*(1), 41–60.

Bousquet, R., Oberhansli, R., Schmid, S., Berger, A., Wiederkeher, M., Robert, C., Moller, A., Rosenberg, C. L., Zeilinger, G., & Molli, G. (2012). *Metamorphic framework of the Alps-Carte metamorphique des Alpes CCGM/CGMW*. CCGM/CGMW.

Brügel, A. (1998). Provenances of Alluvial Conglomerates from the Eastalpine Foreland: Oligo-Miocene Denudation History and Drainage Evolution of the Eastern Alps; 10 Tabellen.

Brügel, A., Dunkl, I., Frisch, W., Kuhlemann, J., & Balogh, K. (2000). The record of Periadriatic volcanism in the Eastern Alpine Molasse zone and its palaeogeographic implications. *Terra Nova*, *12*(1), 42–47.

Brügel, A., Dunkl, I., Frisch, W., Kuhlemann, J., & Balogh, K. (2003). Geochemistry and geochronology of gneiss pebbles from foreland molasse conglomerates: Geodynamic and paleogeographic implications for the Oligo-Miocene evolution of the Eastern Alps. *The Journal of Geology*, *111*(5), 543–563.

Carlson, W. D., Donelick, R. A., & Ketcham, R. A. (1999). Variability of apatite fission-track annealing kinetics: I. Experimental results. *American Mineralogist*, *84*(9), 1213–1223.

Carter, A. (2019). Thermochronology on sand and sandstones for stratigraphic and provenance studies. In M. G. Malusà, & P. G. Fitzgerald (Eds.), *Fission-track thermochronology and its application to geology* (pp. 259–268). Springer.

Chamberlain, K. R., & Bowring, S. A. (2001). Apatite–feldspar U-Pb thermochronometer: A reliable, mid-range (~450° C), diffusion-controlled system. *Chemical Geology*, *172*(1–2), 173–200.

Chew, D., O'Sullivan, G., Caracciolo, L., Mark, C., & Tyrrell, S. (2020). Sourcing the sand: Accessory mineral fertility, analytical and other biases in detrital U-Pb provenance analysis. *Earth-Science Reviews*, *202*, 103093.

Chew, D., Petrus, J., & Kamber, B. (2014). U-Pb LA–ICPMS dating using accessory mineral standards with variable common Pb. *Chemical Geology*, *363*, 185–199.

Chew, D., Sylvester, P. J., & Tubrett, M. N. (2011). U-Pb and Th–Pb dating of apatite by LA-ICPMS. *Chemical Geology*, *280*(1–2), 200–216.

Christensen, J. N., Selverstone, J., Rosenfeld, J. L., & DePaolo, D. J. (1994). Correlation by Rb-Sr geochronology of garnet growth histories from different structural levels within the Tauern Window, Eastern Alps. *Contributions to Mineralogy and Petrology*, *118*(1), 1–12.

Cliff, R., Droop, G., & Rex, D. (1985). Alpine metamorphism in the south-east Tauern Window, Austria: 2. Rates of heating, cooling and uplift. *Journal of Metamorphic Geology*, *3*(4), 403–415.

Covault, J. A., Hubbard, S. M., Graham, S. A., Hinsch, R., & Linzer, H.-G. (2009). Turbidite-reservoir architecture in complex foredeep-margin and wedge-top depocenters, Tertiary Molasse Foreland Basin System, Austria. *Marine and Petroleum Geology*, *26*(3), 379–396.

Cramer, B., Toggweiler, J., Wright, J., Katz, M., & Miller, K. (2009). Ocean overturning since the Late Cretaceous: Inferences from a new benthic foraminiferal isotope compilation. *Paleoceanography*, *24*(4), 1–14.

De Ruig, M. J., & Hubbard, S. M. (2006). Seismic facies and reservoir characteristics of a deep-marine channel belt in the Molasse foreland basin, Puchkirchen Formation, Austria. *AAPG Bulletin*, *90*(5), 735–752.

Del Moro, A., Puxeddu, M., Di Brozolo, F. R., & Villa, I. (1982). Rb-Sr and K-Ar ages on minerals at temperatures of 300–400 C from deep wells in the Larderello geothermal field (Italy). *Contributions to Mineralogy and Petrology*, *81*(4), 340–349.

Dunkl, I., Frisch, W., & Grundmann, G. (2003). Zircon fission track thermochronology of the southeastern part of the Tauern Window and the adjacent Austroalpine margin, Eastern Alps. *Eclogae Geologicae Helvetiae*, *96*(2), 209–218.

Dunkl, I., Frisch, W., Kuhlemann, J., & Brügel, A. (2009). Pebble population dating as an additional tool for provenance studies-examples from the Eastern Alps. *Geological Society, London, Special Publications*, *324*(1), 125–140.

Favaro, S., Handy, M. R., Scharf, A., & Schuster, R. (2017). Changing patterns of exhumation and denudation in front of an advancing crustal indenter, Tauern Window (Eastern Alps). *Tectonics*, *36*(6), 1053–1071.

Favaro, S., Schuster, R., Handy, M. R., Scharf, A., & Pestal, G. (2015). Transition from orogen-perpendicular to orogen-parallel exhumation and cooling during crustal indentation—Key constraints from 147Sm/144Nd and 87Rb/87Sr geochronology (Tauern Window, Alps). *Tectonophysics*, *665*, 1–16.

Foeken, J. P., Persano, C., Stuart, F. M., & Ter Voorde, M. (2007). Role of topography in isotherm perturbation: Apatite (U-Th)/He and fission track results from the Malta tunnel, Tauern Window, Austria. *Tectonics*, *26*(3), 1–15.

Frisch, W., Dunkl, I., & Kuhlemann, J. (2000). Post-collisional orogen-parallel large-scale extension in the Eastern Alps. *Tectonophysics*, *327*(3), 239–265.

Frisch, W., Kuhlemann, J., Dunkl, I., & Brügel, A. (1998). Palinspastic reconstruction and topographic evolution of the Eastern Alps during late Tertiary tectonic extrusion. *Tectonophysics*, *297*(1), 1–15.

Frisch, W., Kuhlemann, J., Dunkl, I., & Székely, B. (2001). The Dachstein paleosurface and the Augenstein Formation in the Northern Calcareous Alps–A mosaic stone in the geomorphological evolution of the Eastern Alps. *International Journal of Earth Sciences*, *90*(3), 500–518.

Füchtbauer, H. (1964). Sedimentpetrographische Untersuchungen in der älteren Molasse nördlich der Alpen. *Eclogae Geologicae Helvetiae*, *57*, 11–289.

Fügenschuh, B., Mancktelow, N. S., & Schmid, S. S. (2012), Comment on Rosenberg and Garcia: estimating displacement along the Brenner Fault and orogen-parallel extension in the Eastern Alps, Int J Earth Sci (Geol Rundsch) (2011) 100: 1129–1145. *International Journal of Earth Sciences*, *101*(5), 1451–1455.

Fügenschuh, B., Mancktelow, N. S., & Seward, D. (2000). Cretaceous to Neogene cooling and exhumation history of the Oetztal-Stubai basement complex, eastern Alps: A structural and fission track study. *Tectonics*, *19*(5), 905–918.

Fügenschuh, B., Seward, D., & Mancktelow, N. (1997). Exhumation in a convergent orogen: The western Tauern window. *Terra Nova*, *9*(5–6), 213–217.

Garver, J. I., Brandon, M. T., Roden-Tice, M., & Kamp, P. J. (1999). Exhumation history of orogenic highlands determined by detrital fission-track thermochronology. *Geological Society, London, Special Publications*, *154*(1), 283–304.

Genser, J., & Neubauer, F. (1989). Low angle normal faults at the eastern margin of the Tauern window (Eastern Alps). *Mitteilungen Der Österreichischen Geologischen Gesellschaft*, *81*(1988), 233–243.

Gleadow, A. (1981). Fission-track dating methods: What are the real alternatives? *Nuclear Tracks*, *5*(1–2), 3–14.

Glodny, J., Ring, U., Kühn, A., Gleissner, P., & Franz, G. (2005). Crystallization and very rapid exhumation of the youngest Alpine eclogites (Tauern Window, Eastern Alps) from Rb/Sr mineral assemblage analysis. *Contributions to Mineralogy and Petrology*, *149*(6), 699–712.

Groß, P., Pleuger, J., Handy, M. R., Germer, M., & John, T. (2021). Evolving temperature field in a fossil subduction channel during the transition from subduction to collision (Tauern Window, Eastern Alps). *Journal of Metamorphic Geology*, *39*, 247–269.

Grundmann, G., & Morteani, G. (1985). The young uplift and thermal history of the central Eastern Alps (Austria/Italy), evidence from apatite fission track ages. *Jahrbuch Der Geologischen Bundesanstalt*, *128*, 197–216.

Grunert, P., Auer, G., Harzhauser, M., & Piller, W. E. (2015). Stratigraphic constraints for the upper Oligocene to lower Miocene Puchkirchen Group (North Alpine Foreland Basin, Central Paratethys). *Newsletters on Stratigraphy*, *48*(1), 111–133.

Grunert, P., Hinsch, R., Sachsenhofer, R. F., Bechtel, A., Ćorić, S., Harzhauser, M., Piller, W. E., & Sperl, H. (2013). Early Burdigalian infill of the Puchkirchen trough (North Alpine Foreland Basin, Central Paratethys): Facies development and sequence stratigraphy. *Marine and Petroleum Geology*, *39*(1), 164–186.

Grunert, P., Soliman, A., Ćorić, S., Roetzel, R., Harzhauser, M., & Piller, W. E. (2012). Facies development along the tide-influenced shelf of the Burdigalian Seaway: An example from the Ottnangian stratotype (Early Miocene, middle Burdigalian). *Marine Micropaleontology*, *84*, 14–36.

Gusterhuber, J., Dunkl, I., Hinsch, R., Linzer, H. G., & Sachsenhofer, R. (2012). Neogene uplift and erosion in the Alpine foreland basin (upper Austria and Salzburg). *Geologica Carpathica*, *63*(4), 295–305.

Gusterhuber, J., Hinsch, R., & Sachsenhofer, R. (2014). Evaluation of hydrocarbon generation and migration in the Molasse fold and thrust belt (Central Eastern Alps, Austria) using structural and thermal basin models. *AAPG Bulletin*, *98*(2), 253–277.

Handy, M. R., Schmid, S. M., Bousquet, R., Kissling, E., & Bernoulli, D. (2010). Reconciling plate-tectonic reconstructions of Alpine Tethys with the geological–geophysical record of spreading and subduction in the Alps. *Earth-Science Reviews*, *102*(3–4), 121–158.

Hawkesworth, C. (1976). Rb/Sr geochronology in the eastern Alps. *Contributions to Mineralogy and Petrology*, *54*(3), 225–244.

Hejl, E., & Grundmann, G. (1989). Apatit-Spaltspurendaten zur thermischen Geschichte der Nördlichen Kalkalpen, der Flysch- und Molassezone. *Jahrbuch Der Geologischen Bundesanstalt*, *132*(1), 191–212.

Henrichs, I. A., O'Sullivan, G., Chew, D., Mark, C., Babechuk, M. G., McKenna, C., & Emo, R. (2018). The trace element and U-Pb systematics of metamorphic apatite. *Chemical Geology*, *483*, 218–238.

Hinsch, R. (2008). New insights into the Oligocene to Miocene geological evolution of the Molasse Basin of Austria. *Oil Gas-European Magazine*, *34*(3), 138–143.

Hinsch, R. (2013). Laterally varying structure and kinematics of the Molasse fold and thrust belt of the Central Eastern Alps: Implications for exploration. *AAPG Bulletin*, *97*(10), 1805–1831.

Hodges, J. L. (1958). The significance probability of the Smirnov two-sample test. *Arkiv För Matematik*, *3*(5), 469–486.

Horváth, F., Bada, G., Szafián, P., Tari, G., Ádám, A., & Cloetingh, S. (2006). Formation and deformation of the Pannonian Basin:

Constraints from observational data. *Geological Society, London, Memoirs*, *32*(1), 191–206.

Hubbard, S. M., de Ruig, M. J., & Graham, S. A. (2009). Confined channel-levee complex development in an elongate depocenter: Deep-water Tertiary strata of the Austrian Molasse basin. *Marine and Petroleum Geology*, *26*(1), 85–112.

Hülscher, J., Fischer, G., Grunert, P., Auer, G., & Bernhardt, A. (2019). Selective Recording of Tectonic Forcings in an Oligocene/Miocene Submarine Channel System: Insights From New Age Constraints and Sediment Volumes From the Austrian Northern Alpine Foreland Basin. *Frontiers in Earth Science*, *7*(302), 1–25.

Hurford, A. J., & Green, P. F. (1983). The zeta age calibration of fission-track dating. *Chemical Geology*, *41*, 285–317.

Inger, S., & Cliff, R. (1994). Timing of metamorphism in the Tauern Window, Eastern Alps: Rb-Sr ages and fabric formation. *Journal of Metamorphic Geology*, *12*(5), 695–707.

Jäger, E. (1967). Die Bedeutung der Biotit-alterswerte. Rb–Sr Alterbestimmungen am Glimmern der Zentralalpen. In E. Jäger, E. Niggli, & E. Wenk (Eds.), *Beiträge zur Geologischen Karte der Schweiz* (Vol. *134*, pp. 28–31).

Jäger, E., Karl, F., & Schmidegg, O. (1969). Rubidium-Strontium-Altersbestimmungen an Biotit-Muskowit-Granitgneisen (Typus Augen-und Flasergneise) aus dem nördlichen Großvenedigerbereich (Hohe Tauern). *Tschermaks Mineralogische Und Petrographische Mitteilungen*, *13*(3–4), 251–272.

Ji, W. Q., Malusà, M. G., Tiepolo, M., Langone, A., Zhao, L., & Wu, F. Y. (2019). Synchronous Periadriatic magmatism in the Western and Central Alps in the absence of slab breakoff. *Terra Nova*, *31*(2), 120–128.

Kohn, B., Chung, L., & Gleadow, A. (2019). Fission-track analysis: Field collection, sample preparation and data acquisition. In *Fission-track thermochronology and its application to geology* (pp. 25–48). Springer.

Krenn, E., Schulz, B., & Finger, F. (2012). Three generations of monazite in Austroalpine basement rocks to the south of the Tauern Window: Evidence for Variscan, Permian and Eo-Alpine Metamorphic Events. *Swiss Journal of Geosciences*, *105*(3), 343–360.

Kuhlemann, J. (2007). Paleogeographic and paleotopographic evolution of the Swiss and Eastern Alps since the Oligocene. *Global and Planetary Change*, *58*(1), 224–236.

Kuhlemann, J., Dunkl, I., Brügel, A., Spiegel, C., & Frisch, W. (2006). From source terrains of the Eastern Alps to the Molasse Basin: Detrital record of non-steady-state exhumation. *Tectonophysics*, *413*(3), 301–316.

Kuhlemann, J., Frisch, W., Dunkl, I., & Székely, B. (2001). Quantifying tectonic versus erosive denudation by the sediment budget: The Miocene core complexes of the Alps. *Tectonophysics*, *330*(1–2), 1–24.

Kuhlemann, J., & Kempf, O. (2002). Post-Eocene evolution of the North Alpine Foreland Basin and its response to Alpine tectonics. *Sedimentary Geology*, *152*(1), 45–78.

Lambert, R. (1970). A potassium-argons study of the margin of the Tauern widow at Dllach, Austria. *Eclogae Geologicae Helveticae*, *63*, 197205.

Linzer, H.-G., Decker, K., Peresson, H., Dell'Mour, R., & Frisch, W. (2002). Balancing lateral orogenic float of the Eastern Alps. *Tectonophysics*, *354*(3–4), 211–237.

Linzer, H.-G., Frisch, W., Zweigel, P., Girbacea, R., Hann, H.-P., & Moser, F. (1998). Kinematic evolution of the Romanian Carpathians. *Tectonophysics*, *297*(1–4), 133–156.

Malusà, M. G., & Fitzgerald, P. G. (2019). Application of thermochronology to geologic problems: Bedrock and detrital approaches. In M. G. Malusà, & P. G. Fitzgerald (Eds.), *Fission-track thermochronology and its application to geology* (pp. 191–209). Springer.

Malusà, M. G., Wang, J., Garzanti, E., Liu, Z.-C., Villa, I. M., & Wittmann, H. (2017). Trace-element and Nd-isotope systematics in detrital apatite of the Po river catchment: Implications for provenance discrimination and the lag-time approach to detrital thermochronology. *Lithos*, *290*, 48–59.

Martin, S., Prosser, G., & Morten, L. (1993). Tectono-magmatic evolution of sheeted plutonic bodies along the north Giudicarie line (northern Italy). *Geologische Rundschau*, *82*(1), 51–66.

Masalimova, L. U., Lowe, D. R., Mchargue, T., & Derksen, R. (2015). Interplay between an axial channel belt, slope gullies and overbank deposition in the Puchkirchen Formation in the Molasse Basin, Austria. *Sedimentology*, *62*(6), 1717–1748.

McDowell, F. W., McIntosh, W. C., & Farley, K. A. (2005). A precise 40Ar–39Ar reference age for the Durango apatite (U–Th)/He and fission-track dating standard. *Chemical Geology*, *214*(3–4), 249–263.

Miller, C., & Thöni, M. (1995). Origin of eclogites from the Austroalpine Ötztal basement (Tirol, Austria): Geochemistry and Sm-Nd vs. Rb-Sr isotope systematics. *Chemical Geology*, *122*(1–4), 199–225.

Mosbrugger, V., Utescher, T., & Dilcher, D. L. (2005). Cenozoic continental climatic evolution of Central Europe. *Proceedings of the National Academy of Sciences of the United States of America*, *102*(42), 14964–14969.

Most, P. (2003). *Late Alpine cooling histories of tectonic blocks along the central part of the Transalp-Traverse (Inntal-Gadertal): Constraints from geochronology* [PhD]. Eberhardt-Karls-Universität Tübingen.

Müller, W., Mancktelow, N. S., & Meier, M. (2000). Rb–Sr microchrons of synkinematic mica in mylonites: An example from the DAV fault of the Eastern Alps. *Earth and Planetary Science Letters*, *180*(3–4), 385–397.

Müller, W., Prosser, G., Mancktelow, N. S., Villa, I. M., Kelley, S. P., Viola, G., & Oberli, F. (2001). Geochronological constraints on the evolution of the Periadriatic Fault System (Alps). *International Journal of Earth Sciences*, *90*(3), 623–653.

Naeser, C. (1979). Fission-track dating and geologic annealing of fission tracks. In E. Jäger, & J. C. Hunziker (Eds.), *Lectures in isotope geology* (pp. 154–169). Springer.

Ortner, H., Aichholzer, S., Zerlauth, M., Pilser, R., & Fügenschuh, B. (2015). Geometry, amount, and sequence of thrusting in the Subalpine Molasse of western Austria and southern Germany, European Alps. *Tectonics*, *34*(1), 1–30.

Ortner, H., Reiter, F., & Brandner, R. (2006). Kinematics of the Inntal shear zone–sub-Tauern ramp fault system and the interpretation of the TRANSALP seismic section, Eastern Alps, Austria. *Tectonophysics*, *414*(1–4), 241–258.

Ortner, H., & Stingl, V. (2001). Facies and basin development of the Oligocene in the Lower Inn Valley, Tyrol/Bavaria, Wien. Österreichische Akademie der Wissenschaften, Schriftreihe der Erdwissenschaftlichen Kommision, Paleogene of the Eastern Alps (Vol. *14*).

O'Sullivan, G., Chew, D., Kenny, G., Henrichs, I., & Mulligan, D. (2020). The trace element composition of apatite and its application to detrital provenance studies. *Earth-Science Reviews*, *201*, 103044.

O'Sullivan, G., Chew, D., Morton, A., Mark, C., & Henrichs, I. (2018). An integrated apatite geochronology and geochemistry tool for sedimentary provenance analysis. *Geochemistry, Geophysics, Geosystems*, *19*(4), 1309–1326.

Oxburgh, E., Lambert, R. S. J., Baadsgaard, H., & Simons, J. (1966). *Potassium argon age studies across the south-east margin of the Tauern Window, the Eastern Alps* (Vol. *1966*, pp. 17–33). Verhandlungen der Geologischen Bundesanstalt.

Paton, C., Hellstrom, J., Paul, B., Woodhead, J., & Hergt, J. (2011). Iolite: Freeware for the visualisation and processing of mass spectrometric data. *Journal of Analytical Atomic Spectrometry*, *26*(12), 2508–2518.

Pomella, H., Klötzli, U., Scholger, R., Stipp, M., & Fügenschuh, B. (2011). The Northern Giudicarie and the Meran-Mauls fault (Alps, Northern Italy) in the light of new paleomagnetic and geochronological data from boudinaged Eo-/Oligocene tonalites. *International Journal of Earth Sciences*, *100*(8), 1827–1850.

Pomella, H., Stipp, M., & Fügenschuh, B. (2012). Thermochronological record of thrusting and strike-slip faulting along the Giudicarie fault system (Alps, Northern Italy). *Tectonophysics*, *579*, 118–130.

Prosser, G. (1998). Strike-slip movements and thrusting along a transpressive fault zone: The North Giudicarie line (Insubric line, northern Italy). *Tectonics*, *17*(6), 921–937.

Prosser, G. (2000). The development of the North Giudicarie fault zone (Insubric line, Northern Italy). *Journal of Geodynamics*, *30*(1–2), 229–250.

Purdy, J., & Jäger, E. (1976). *K-Ar ages on rock-forming minerals from the Central Alps* (Vol. *30*). Memorie degli Instituti di Geologia e Mineralogia dell'Universitá di Padova.

Raith, M., Raase, P., Kreuzer, H., & Müller, P. (1978). The age of the Alpidic metamorphism in the western Tauern Window, Austrian Alps, according to radiometric dating. In H. Closs, D. Roeder, & K. Schmidt (Eds.), *Alps, Apennines, Hellenides* (Vol. *38*, pp. 140–148). Inter-Union Comm Geodynamics Sci Rep.

Ratschbacher, L., Dingeldey, C., Miller, C., Hacker, B. R., & McWilliams, M. O. (2004). Formation, subduction, and exhumation of Penninic oceanic crust in the Eastern Alps: Time constraints from 40Ar/39Ar geochronology. *Tectonophysics*, *394*(3–4), 155–170.

Ratschbacher, L., Frisch, W., Linzer, H. G., & Merle, O. (1991). Lateral extrusion in the Eastern Alps, part 2: Structural analysis. *Tectonics*, *10*(2), 257–271.

Reddy, S., Cliff, R., & East, R. (1993). Thermal history of the Sonnblick Dome, south-east Tauern Window, Austria: Implications for heterogeneous uplift within the Pennine basement. *Geologische Rundschau*, *82*(4), 667–675.

Reiners, P. W., & Brandon, M. T. (2006). Using thermochronology to understand orogenic erosion. *Annual Review of Earth and Planetary Sciences*, *34*, 419–466.

Roddick, J., Cliff, R., & Rex, D. (1980). The evolution of excess argon in alpine biotites—A40Ar-39Ar analysis. *Earth and Planetary Science Letters*, *48*(1), 185–208.

Rode, S., Rösel, D., & Schulz, B. (2012). Constraints on the Variscan PT evolution by EMP Th-U-Pb monazite dating in the polymetamorphic Austroalpine Oetztal-Stubai basement (Eastern Alps). *Zeitschrift Der Deutschen Gesellschaft Für Geowissenschaften*, *163*(1), 43–67.

Rögl, F., Hochuli, P., & Muller, C. (1979). Oligocene–early Miocene stratigraphic correlations in the Molasse Basin of Austria. Annales Geologiques des Pays Helleniques. Tome Hors Series, *30*, 1045–1050.

Rosenberg, C. L., & Berger, A. (2009). On the causes and modes of exhumation and lateral growth of the Alps. *Tectonics*, *28*(6), 1–16.

Rosenberg, C. L., Brun, J. P., Cagnard, F., & Gapais, D. (2007). Oblique indentation in the Eastern Alps: Insights from laboratory experiments. *Tectonics*, *26*(2).

Rosenberg, C. L., & Garcia, S. (2011). Estimating displacement along the Brenner Fault and orogen-parallel extension in the Eastern Alps. *International Journal of Earth Sciences*, *100*(5), 1129–1145.

Rosenberg, C. L., & Kissling, E. (2013). Three-dimensional insight into Central-Alpine collision: Lower-plate or upper-plate indentation? *Geology*, *41*(12), 1219–1222.

Rosenberg, C. L., & Schneider, S. (2008). The western termination of the SEMP Fault (eastern Alps) and its bearing on the exhumation of the Tauern Window. *Geological Society, London, Special Publications*, *298*(1), 197–218.

Rosenberg, C. L., Schneider, S., Scharf, A., Bertrand, A., Hammerschmidt, K., Rabaute, A., & Brun, J.-P. (2018). Relating collisional kinematics to exhumation processes in the Eastern Alps. *Earth-Science Reviews*, *176*, 311–344.

Royden, L. H. (1988). Late Cenozoic Tectonics of the Pannonian Basin System: Chapter 3.

Satir, M. (1976). Rb-Sr-und K-Ar-Altersbestimmungen an Gesteinen und Mineralien des südlichen Ötztalkristallins und der westlichen Hohen Tauern. *Geologische Rundschau*, *65*(1), 394–410.

Satir, M., & Morteani, G. (1982). Petrological study and radiometric age determination of the migmatites in the Penninic rocks of the Zillertaler Alpen (Tyrol/Austria). *Tschermaks Mineralogische Und Petrographische Mitteilungen*, *30*(1), 59–75.

Scharf, A., Handy, M. R., Favaro, S., Schmid, S. M., & Bertrand, A. (2013). Modes of orogen-parallel stretching and extensional exhumation in response to microplate indentation and roll-back subduction (Tauern Window, Eastern Alps). *International Journal of Earth Sciences*, *102*(6), 1627–1654.

Scharf, A., Handy, M. R., Ziemann, M. A., & Schmid, S. M. (2013). Peak-temperature patterns of polyphase metamorphism resulting from accretion, subduction and collision (eastern Tauern Window, European Alps)–A study with Raman microspectroscopy on carbonaceous material (RSCM). *Journal of Metamorphic Geology*, *31*(8), 863–880.

Schmid, S. M., Fügenschuh, B., Kissling, E., & Schuster, R. (2004). Tectonic map and overall architecture of the Alpine orogen. *Eclogae Geologicae Helvetiae*, *97*(1), 93–117.

Schmid, S. M., Scharf, A., Handy, M. R., & Rosenberg, C. L. (2013). The Tauern Window (Eastern Alps, Austria): A new tectonic map, with cross-sections and a tectonometamorphic synthesis. *Swiss Journal of Geosciences*, *106*(1), 1–32.

Schneider, S., Hammerschmidt, K., & Rosenberg, C. L. (2013). Dating the longevity of ductile shear zones: Insight from 40Ar/39Ar in situ analyses. *Earth and Planetary Science Letters*, *369*, 43–58.

Schneider, S., Hammerschmidt, K., Rosenberg, C. L., Gerdes, A., Frei, D., & Bertrand, A. (2015). U-Pb ages of apatite in the

western Tauern Window (Eastern Alps): Tracing the onset of collision-related exhumation in the European plate. *Earth and Planetary Science Letters*, *418*, 53–65.

Schoene, B., & Bowring, S. A. (2006). U-Pb systematics of the McClure Mountain syenite: Thermochronological constraints on the age of the 40 Ar/39 Ar standard MMhb. *Contributions to Mineralogy and Petrology*, *151*(5), 615.

Schulz, B., Krause, J., & Zimmermann, R. (2019). Electron microprobe petrochronology of monazite-bearing garnet micaschists in the Oetztal-Stubai Complex (Alpeiner Valley, Stubai). *Swiss Journal of Geosciences*, *112*(2–3), 597–617.

Schuster, R., Scharbert, S., Abart, R., & Frank, W. (2001). Permo-Triassic extension and related HT/LP metamorphism in the Austroalpine-Southalpine realm. Mitteilungen der Gesellschaft der Geologie- und Bergbaustudenten in Österreich, *45*, 111–141.

Schuster, R., Tropper, P., Krenn, E., Finger, F., Frank, W., & Philippitsch, R. (2015). Prograde Permo-Triassic metamorphic HT/LP assemblages from the Austroalpine Jenig Complex (Carinthia, Austria). *Austrian Journal of Earth Sciences*, *108*(1), 73–90.

Selverstone, J. (1988). Evidence for east-west crustal extension in the Eastern Alps: Implications for the unroofing history of the Tauern Window. *Tectonics*, *7*(1), 87–105.

Sharman, G. R., Hubbard, S. M., Covault, J. A., Hinsch, R., Linzer, H.-G., & Graham, S. A. (2018). Sediment Routing Evolution in the Northern Alpine Foreland Basin, Austria: Interplay of transverse and longitudinal sediment dispersal. *Basin Research*, *30*(3), 426–447.

Skeries, W., & Troll, G. (1991). Der Geröllbestand in Molassekonglomeraten des Chiemgaus (Bayern) und seine paläogeographischen Beziehungen zum alpinen Liefergebiet. *Zeitschrift Der Deutschen Geologischen Gesellschaft*, *142*, 43–66.

Spiegel, C., Kuhlemann, J., Dunkl, I., & Frisch, W. (2001). Paleogeography and catchment evolution in a mobile orogenic belt: The Central Alps in Oligo-Miocene times. *Tectonophysics*, *341*(1–4), 33–47.

Stacey, J. T., & Kramers, J. (1975). Approximation of terrestrial lead isotope evolution by a two-stage model. *Earth and Planetary Science Letters*, *26*(2), 207–221.

Staufenberg, H. (1987). Apatite fission-track evidence for postmetamorphic uplift and cooling history of the Eastern Tauern Window and the surrounding Austroalpine (Central Eastern Alps, Austria). *Jahrbuch Der Geologischen Bundesanstalt*, *130*, 571–586.

Stefani, C., Fellin, M. G., Zattin, M., Zuffa, G. G., Dalmonte, C., Mancin, N., & Zanferrari, A. (2007). Provenance and paleogeographic evolution in a multi-source foreland: The Cenozoic Venetian-Friulian Basin (NE Italy). *Journal of Sedimentary Research*, *77*(11), 867–887.

Thomson, S. N., Gehrels, G. E., Ruiz, J., & Buchwaldt, R. (2012). Routine low-damage apatite U-Pb dating using laser ablation–multicollector–ICPMS. *Geochemistry, Geophysics, Geosystems*, *13*(2), 1–23.

Thöni, M., & Miller, C. (2000). Permo-Triassic pegmatites in the eo-Alpine eclogite-facies Koralpe complex, Austria: Age and magma source constraints from mineral chemical. Rb-Sr and Sm-Nd isotope data. *Schweizerische Mineralogische Und Petrographische Mitteilungen*, *80*(2), 169–186.

Vermeesch, P. (2009). RadialPlotter: A Java application for fission track, luminescence and other radial plots. *Radiation Measurements*, *44*(4), 409–410.

Verwater, V. F., Le Breton, E., Handy, M. R., Picotti, V., Jozi Najafabadi, A., & Haberland, C. (2021). Neogene kinematics of the Giudicarie Belt and eastern Southern Alpine orogenic front (northern Italy). *Solid Earth*, *12*(6), 1309–1334.

Wolff, R., Hetzel, R., Dunkl, I., Anczkiewicz, A. A., & Pomella, H. (2020). Fast cooling of normal-fault footwalls: Rapid fault slip or thermal relaxation? *Geology*, *48*, 333–337.

Zattin, M., Stefani, C., & Martin, S. (2003). Detrital fission-track analysis and sedimentary petrofacies as keys of alpine exhumation: The example of the Venetian Foreland (European Southern Alps, Italy). *Journal of Sedimentary Research*, *73*(6), 1051–1061.

Zimmermann, R., Hammerschmidt, K., & Franz, G. (1994). Eocene high pressure metamorphism in the Penninic units of the Tauern Window (Eastern Alps): Evidence from 40 Ar— 39 Ar dating and petrological investigations. *Contributions to Mineralogy and Petrology*, *117*(2), 175–186.

Zweigel, J. (1998). Eustatic versus tectonic control on foreland basin fill. *Contributions to Sedimentary Geology*, *20*, 1–140.

SUPPORTING INFORMATION

Additional Supporting Information may be found online in the Supporting Information section.

How to cite this article: Hülscher, J., Sobel, E. R., Verwater, V., Groß, P., Chew, D., & Bernhardt, A. (2021). Detrital apatite geochemistry and thermochronology from the Oligocene/Miocene Alpine foreland record the early exhumation of the Tauern Window. *Basin Research*, 33, 3021–3044. https://doi.org/10.1111/bre.12593